MASTER THESIS:
BIOMEDICAL ENGINEERING
PHYSIOLOGICAL SIGNALS & SYSTEMS

QUANTIFICATION OF AEROSOL DEPOSITION IN THE NASAL CAVITY

M. SCHEEREN

2024

Supervisors

Dr.ir. F.H.C. de Jongh
University of Twente

F. Verhoeven
Medspray B.V.

Committee Chairman

Prof.dr.ir. C.H. Venner
University of Twente

External Committee Member

Prof.dr.ir. R.M. Verdaasdonk
University of Twente

medspray

UNIVERSITY OF TWENTE.

Preface

Before you lies the Master thesis: "Quantification of Aerosol Deposition in the Nasal Cavity". This paper was part of the track Physiological Signals and Systems of Biomedical Engineering (BME). The research was conducted for and at Medspray B.V. as part of the development of the soft mist nozzle for nasal sprays. Under the supervision of F. Verhoeven and F.H.C. de Jongh, the study was conducted from August 2023 to June 2024.

This work is the culmination of many years of education. Starting in 2010 with the Bachelor of Technical Medicine (TM), I began this thesis with the help of F.H.C. de Jongh and A. Dekker-Drummer at Medspray B.V., aiming to complete my Master's program. Through my various internships under the supervision of F.H.C. de Jongh, I received invaluable advice that helped me grow as a professional. I would like to thank him for his time and understanding of my personal circumstances. Additionally, I appreciate his efforts in connecting me with Medspray B.V. to conduct my thesis there. A. Dekker-Drummer provided crucial guidance during my transition from the Master in TM to BME. Her advice and support helped me find my place and manage all necessary administrative tasks. Her reminders to take care of myself alleviated the pressure during tough times. As well as special thanks to D. Brandwagt for all her support during my time at TM.

At Medspray B.V., I found a warm and welcoming atmosphere, for which I am very grateful. I would like to give special appreciation to several people. F. Verhoeven for the numerous hours spent providing feedback and for our many valuable conversations. S. van der Vegte took on the role of daily supervisor during F. Verhoeven's paternity leave, offered an external perspective that kept the project's goals in sight. P. Ravensbergen helped me develop, set up, and conduct the experiments for this thesis, and his enthusiasm motivated me during challenging times. I. Oenes assisted with the necessary contract filings and A. Mollink provided much-appreciated hallway conversations that allowed me to express my thoughts and feelings. I would also like to thank everyone who shared good conversations during lunches and breaks. Their company made me feel at home during this thesis.

I also want to acknowledge my support network. Friends who listened to my problems and provided welcome distractions during tough times were invaluable. I extend special thanks to my uncle, B. de Jong, for his valuable external feedback on the clarity of my writing. My family's support in various ways has enabled me to reach this point. Though my mother, who sadly passed in January 2024, cannot witness the culmination of her support, she remains close to my heart, knowing she was proud of me. Finally, I thank my partner, M.R. Magnée, who supported me unconditionally. Her support enabled me to face difficult times and focus on my work.

This thesis marks the end of one chapter of my life and the beginning of my future. I hope readers find this thesis insightful and I thank you for taking the time to read my work.

Mark Scheeren

Enschede, 24-06-2024

Abstract

Introduction: Nasal sprays are currently used to administer local nasal medication for congestion and allergies. However, due to the nasal anatomy, they are also a viable site for broader medication administration, utilizing both high vascularization and nose-to-brain pathways. To leverage these capabilities, Medspray developed a soft mist nasal spray. Quantifying aerosol deposition is essential to evaluate nasal spray effectiveness and investigate volume distribution.

Method: Using the fluorescent properties of calcein, a photo analytic program was developed to quantify aerosol deposition in a nasal cast created by Koken. The algorithm calculates the volume of aerosol deposition by calibrating the intensity of emission to the thickness of the deposition.

Results: The algorithm calculated the volume of deposition with approximately 20% deviation. This allowed insight into how the volume is distributed in the nasal cavity. When comparing a traditional swirl nozzle to the soft mist nozzle, the traditional swirl nozzle deposited 85% of the volume on a surface area of 80 mm², while the soft mist nozzle deposited 73% on a surface area of 148 mm². The remaining 15% and 27% were spread over surface areas of 1766 mm² and 2082 mm², respectively.

Discussion: The developed algorithm can quantify aerosol dispersion, providing insight into volume distribution in the nasal cavity and enabling further study of parameters affecting nasal sprays. Artefacts during calibration and measurement affect accuracy and require further investigation to improve this approach.

Conclusion: Photo analysis can quantify nasal deposition in an in vitro environment, providing valuable data on aerosol distribution in the nasal cavity. It also demonstrates differences in deposition between the standard swirl nozzle and the soft mist nozzle, with the former creating thicker focal points and the latter offering a more evenly spread distribution.

Table of Contents

1. Introduction

There are multiple manners in which medication is applied for both daily use and emergency care. The most common method of medication administration is oral, which provides systemic delivery. Another approach is an injection for direct entry to the bloodstream, however, this is an invasive method. Nasal spray is currently used to administer the liquids for local antihistamines and corticosteroids in the nose. Nevertheless, given the anatomical structures within the nose, it is also feasible to administer other medications via nasal spray.[1]

The nose comprises two cavities, which can be subdivided into three distinct regions, as illustrated in Figure 1: the nasal vestibule, respiratory region, and olfactory region. The nasal vestibule serves as the nose's primary filter, with the first half covered with vibrissae and the second half in respiratory epithelium. Moving deeper, the respiratory region is lined with ciliated pseudostratified epithelium and mucous cells, facilitating air humidification, and warming before it reaches the lungs. Furthermore, within this region are three curved shelves of bone known as the superior, middle, and inferior turbinates, protruding from the cavity's lateral walls. The turbinates slow the airflow to increase the level of filtration, humidification, and heating done in the respiratory region. The final region is the olfactory region which is covered with olfactory epithelium, sensory cilia, and mucosa.[2,3]
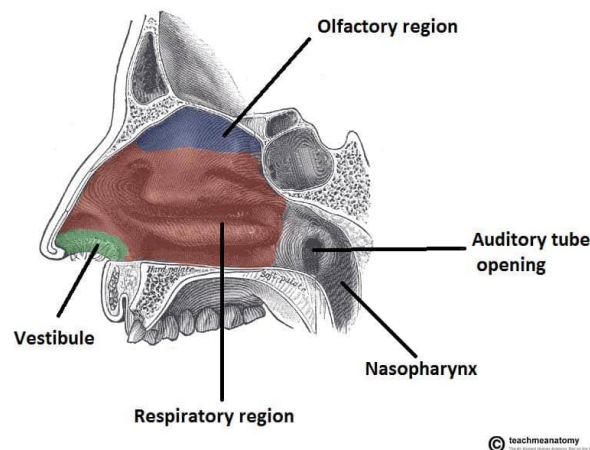
Figure 1: Anatomical representation of the nose[2]

The olfactory mucosa is directly connected to the brain through the olfactory pathways, enabling drugs to bypass the blood-brain barrier and gain direct access to the central nervous system[4,5]. This feature makes it possible for drugs to be administered daily as a replacement for oral intake, which is limited due to side effects [6–11]. Utilization of this site extends beyond medication; vaccination can also be administered via this route[12,13]. However, to establish these regions as viable administration sites, it is crucial to quantify medication deposition in these areas.

The current technology most used for the delivery of nasal medication is spray pumps[1]. However, a significant portion of the contents is deposited in the nasal vestibule, a region considered unattractive for aerosol deposition due to its filtration function and potential for leakage. One likely reason for aerosol deposition being limited to that region is the inertial impaction of particles with a volume median particle size (dv50) greater than 50 μm, emitted at high velocity[14–16]. However,

several other factors, such as anatomy and technique, also contribute to this limitation in dispersion beyond droplet size and velocity, thus reducing delivery effectiveness[17,18].

It is important to understand the characteristics of nasal products to determine the desired delivery outcomes[19]. However, there are currently no standard guidelines for the evaluation of nasal deposition.[20,21] Several studies have utilized silicone nasal cavity models to visualize deposition patterns. Transparent silicon models, such as the Optinose® and Koken® nasal cast models allow for good visualization of aerosol deposition patterns[22,23].

With the Koken model, it has been demonstrated that, while originally designed for education, it serves as an effective tool for visualizing the behaviour of both powder and liquid formulations.[23] In these experiments, water-finding colour-changing gels or pastes were applied to highlight regions where the liquid formulation was deposited. Kundoor and Dalby validated the use of Sar-Gel® and studied the deposition of three different commercial products with and without vacuum pumps. Another water-finding gel is Kolor-Kut®, which was used successfully by Lungare, Bowen, and Badhan to execute a deposition study on the Koken cast model.[24] Figure 2 illustrates how Kolor-Kut displays the distribution pattern of the aerosol solution, changing from yellow to deep red, and from dry to wet respectively. However, it was found that these gels had low sensitivity and experienced interference from humidity. Additionally, the paste was found challenging to apply evenly across the model. [1]
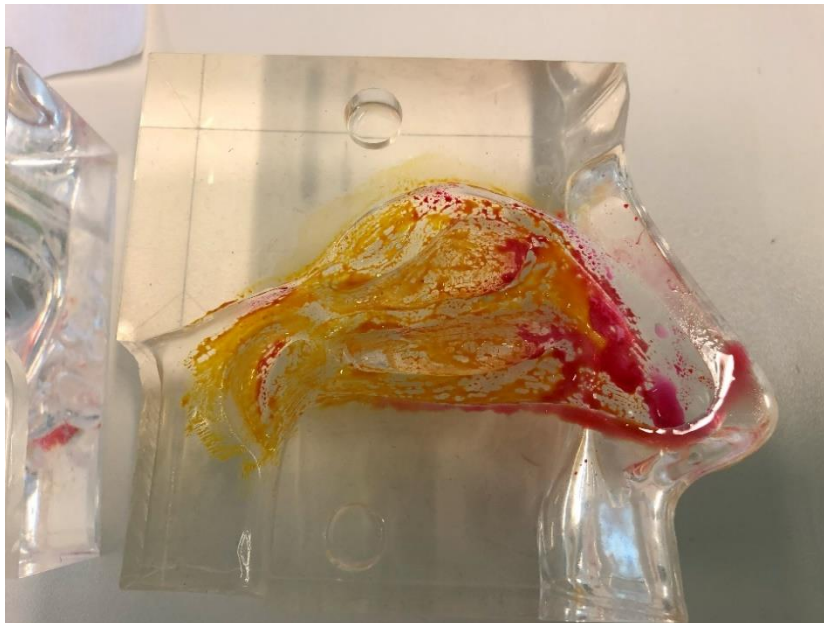
Figure 2: Model coated with Kolor-Kut and showing the colour distribution after nose spray application.[24]

D'Angelo, Kooij, and Verhoeven et al. applied fluorescence to visualize and quantify the deposition coverage of a nasal liquid formulation, as depicted in Figure 3.[1] Through this study, it was possible to determine the area covered by a pump fitted with Medspray's innovative design nozzle, which utilizes the soft mist principle. This nozzle emits a spray consisting of a narrow droplet size distribution with Dv50 between 15 and 25 μm at a low spray velocity. The fluorescence was achieved by excitation through a UV lamp with a wavelength of 366 nm.[1]
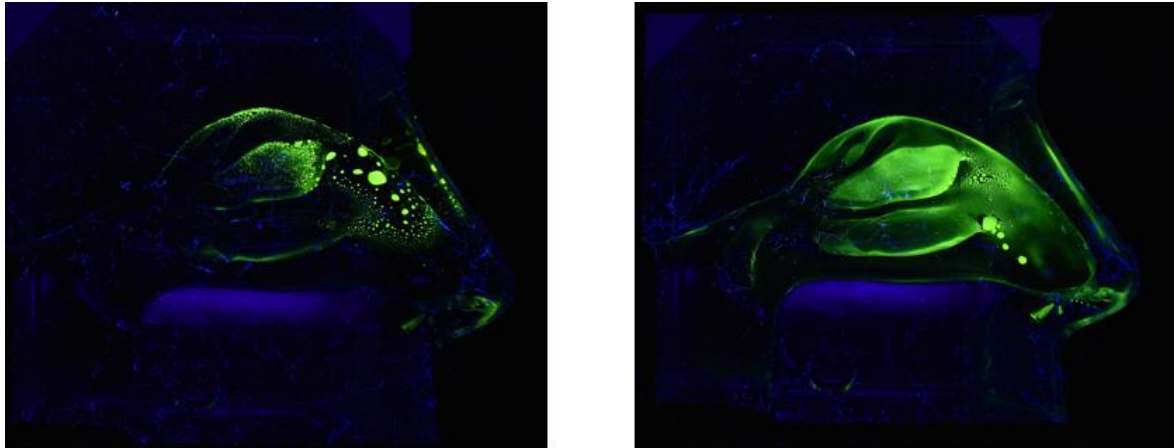
Figure 3: shows the excitation of calcein using UV light. The left displays a standard nozzle, and the right demonstrates the distribution of the Medspray nozzle.[1]

This method employs UV light within a dark box to excite the fluorescent dye in the solution, thereby inducing fluorescence that facilitates visualization of concentration. This setup minimizes background interference, as the images are captured in a black box illuminated by a singular light source. While these approaches focus on visualizing the aerosol dispersal pattern, quantification using these methods has proven more challenging.[19] This study hypothesizes that the colour gradient can be correlated to the quantity of the dispersal of the aerosol through the nose.

A model suitable for quantification is the Alberta Idealised Nasal Inlet model (AINI), depicted in Figure 4. Having each nasal region as a separate module that can be detached from the AINI model, makes it possible to analyse each compartment separately.[25] The most common approach involves washing out the compartment into cuvettes, which enables spectroscopy. Spectroscopy utilizes the absorption spectrum to analyse particles in a solution. For instance, UV-VIS spectroscopy is a method that employs ultraviolet and visible light to probe the electronic structure of molecules present in a sample, facilitating precise quantification of the molecules in the sample. [26] A limitation of this method is that it requires the removal of the substance from the model.
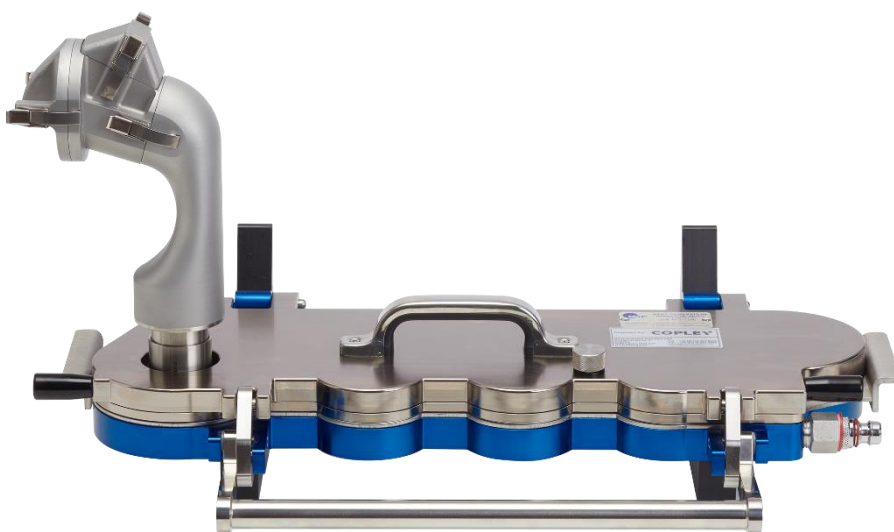
Figure 4: The Alberta Idealised Nasal Inlet (AINI) model.[25]

The objective of this research is to develop a method for quantifying the dispersal of aerosols throughout the nasal cavity while allowing for visual inspection of the same model. To optimize the use of nasal sprays, it is essential to not only understand how they cover the nasal cavity but also to determine the required quantity. This investigation aims to assess the comparative effectiveness of the soft mist nasal spray from Medspray compared to a standard nozzle. In evaluating aerosol deposition with different nozzle types, it is equally important to identify external factors influencing dispersion, such as spray velocity, droplet size, room temperature, and inhalation flow. Therefore, this study aims to comprehensively explore these factors and other parameters affecting the functionality of the soft mist nasal spray device.

Boundary conditions may restrict access to specific regions, prompting an inquiry to identify the influencing factors on dispersion. Additionally, external factors can significantly affect the accuracy of the quantification method. Hence, minimizing these external factors and boundary conditions is essential for ensuring reliable quantification.

Currently, there are no standard guidelines for determining effective nasal delivery of medical aerosol. With a quantification method that enables visual inspection of the same model, calculations can be performed to determine the necessary nasal spray quantity to achieve the desired dosage for the target area. This paper aims to provide the tools necessary to establish such guidelines.

2. Background

2.1 Nasal anatomy

The nose is a complex anatomical region that begins with the nostrils leading into the nasal vestibule. Serving primarily as a filter for the respiratory system, the nasal vestibule comprises two distinct parts. The first half is covered with keratinized stratified squamous epithelium that contains coarse hairs called vibrissae, which filter inhaled particles. The second half is lined with pseudostratified ciliated columnar epithelium, a form of respiratory epithelium. This epithelium serves to moisturize incoming air and acts as a physical barrier against pathogens.[3]

After the nasal vestibule, the next section that is encountered is the respiratory region, which primarily functions to humidify, warm, filter, protect, and eliminate debris[27]. Similar to the second part of the nasal vestibule, the respiratory region is covered with respiratory epithelium. Additionally, it is lined with mucous cells, enhancing its filter function compared to the nasal vestibule.[3] Debris captured in the mucous cells is removed through the mucociliary system, where the pseudostratified ciliated columnar epithelium has a clearance rate of one centimetre per second.[27] Immunoglobulin A, lysozymes, and lactoferrin present in the mucosa neutralize inhaled pathogens.[3] The inhaled air is humidified to 100% and warmed to body temperature.[2] To aid the respiratory region, the neurovascular system controls the lower turbinate and anterior septum by controlling the blood volume in the erectile tissue. Under normal conditions, the superior cervical ganglia keep the cavity uncongested.[3]

The third region, situated at the apex of the nose, is the olfactory region. This region is supplied by either orthonasal or retronasal flow, through which odour-carrying particles reach the olfactory epithelium. These odorants become trapped in the olfactory mucus, where they attach to odour-binding proteins.[3] These proteins concentrate and aid in solubilizing the particles. Once attached to olfactory receptors on cilia, the odorants transmit specific signals up through the cribriform plate to synapse with neurons in the olfactory bulb.[17] Subsequently, the olfactory bulb sends signals to the olfactory nerve, which then relays them to secondary neurons for further processing before reaching the brain.[2]

2.2 Nasal medication

2.2.1 Local and Systemic Delivery

To be adequately absorbed, medication must penetrate multiple layers of the nasal structure, consisting of four main cell types: basal cells, goblet cells, ciliated columnar cells, and non-ciliated cells. Basal cells are exclusively found in the basement membrane, while the other three cell types are distributed across the entire apical epithelial surface.[28]

The first layer, the mucosa, serves as a protective barrier for the nose and consists of epithelium, basement membrane, and lamina propria.[29] Adequate delivery of medication requires control over the release curve. The cilia quickly clear foreign material, emphasizing the importance of rapid absorption through the initial mucosal layer.[28] Subsequently, drugs primarily penetrate the epithelial cell membrane through cross-diffusion. They then pass through the stroma and basement membrane, ultimately reaching the targeted area for local medication delivery.[29] This method is

preferred for antihistamines and corticosteroids due to their safety profile. Salib and Howarth found fewer systemic adverse effects when analysing the safety of nasal inhalation compared to oral intake, mainly attributed to the lower dosage required for therapeutic effect.[30]

Systemic delivery encounters an additional barrier: the capillary endothelium, as the mucosa layer is highly vascularised. These barriers are less aggressive than the hepatogastrointestinal filter, resulting in similarly lower dosages required for therapeutic effects. However, this route is only viable for medication with aqueous solubility, as it necessitates absorption into the mucosal layer.[28]

2.2.2 Nose-to-Brain Delivery

A barrier is formed between the brain and the blood supplying oxygen to neurons to protect the brain from harmful substances. This barrier allows cerebral blood vessels to filter and regulate molecule and ion movement between the blood and the brain, which can cause difficulties when trying to supply medication to the brain. This filter can be partially bypassed using the unique connection of the olfactory region to the brain. [31]

This works through three possible pathways. The first pathway is the olfactory pathway. Drugs reaching the olfactory epithelium can be transported to the olfactory bulb. Different routes for transport can transfer the drug into the brain. Intracellular transport pathway after the drug's internalization into neurons is the first route that can be used. Secondly, extracellular transport across intercellular spaces, and finally intercellular transport across basal epithelial cells. [32]

The second pathway is the trigeminal pathway. This uses the trigeminal nerve, which innervates the olfactory epithelium and mucosa, allowing for an additional but less important pathway for direct drug transport. Due to not being able to accurately measure, because part of the trigeminal nerve enters the brain through the sieve plate, which is adjacent to the olfactory pathway.[32]

The final pathway is the peripheral pathway. Here drugs enter the vascular systemic circulation and enter the brain through the blood-brain barrier. The benefit of bypassing the hepatogastrointestinal filter is that the kidneys filter the systemic absorption and additional systemic effects may occur. Which makes this pathway the least desirable nose-to-brain bridge.[32]

N2B allows medication to bypass some of the intense filters, enabling the drug to be administered in lower dosages for similar effects. [31] Neurological diseases such as Alzheimer's, Parkinson's and migraine are examples that can be treated more effectively using these pathways. [33–35] However, the N2B connection can also be used for medication that needs to be administered daily such as with ADHD, cancer, and depression.[36–38] Combining the systemic capabilities of the nose with the nose-to-brain pathways, it becomes possible to trigger an immune response and administer vaccinations in this less invasive manner.[39]

With these capabilities of the nose as an administration site for medication it becomes apparent that it is necessary to find methods to safely apply the desired therapeutic dose in this area. Currently, nasal sprays are the viable method of directly applying the medication to the nasal cavity.

2.3 Nozzle mechanisms

Nasal sprays consist of several components. The first part includes the pump with the liquid container, while the second part is the actuator containing the nozzle, also known as the spray nozzle, insert (SNI).[40] In the commonly used nasal sprays, a swirl nozzle is employed. This unit utilizes a spring to pump the liquid into a cylindrical chamber with a velocity of 15 to 20 m/s.[1] As the liquid swirls within the chamber, it is pushed against the wall and directed toward the small exit on top of the nozzle.[40] Upon exiting the orifice, the surface tension, combined with the high velocity, breaks the fluid apart into small droplets, resulting in a cone-like spray pattern with a volume median particle size (Dv50) typically greater than 50 μm.[1] This cone-like spray is shown in Figure 5A. Most of these droplets are distributed in the nasal vestibule.

In contrast, the soft mist spray uses a different mechanism to create a plume. It utilizes the Rayleigh principle, first described by Lord Rayleigh, to break up a jet by inducing instability caused by pushing the jet through a filter and mesh.[41] These small openings fragment the liquid into smaller droplets, creating a soft mist cloud with a low velocity of around 0.8 m/s. Unlike with a swirl nozzle, the Dv50 is between 15 and 25 μm. Due to the smaller droplet size and the significantly lower velocity upon exiting the nozzle, a more plume-like jet is produced, as can be seen in Figure 5C, facilitating deeper penetration of droplets into the nasal region.[1]
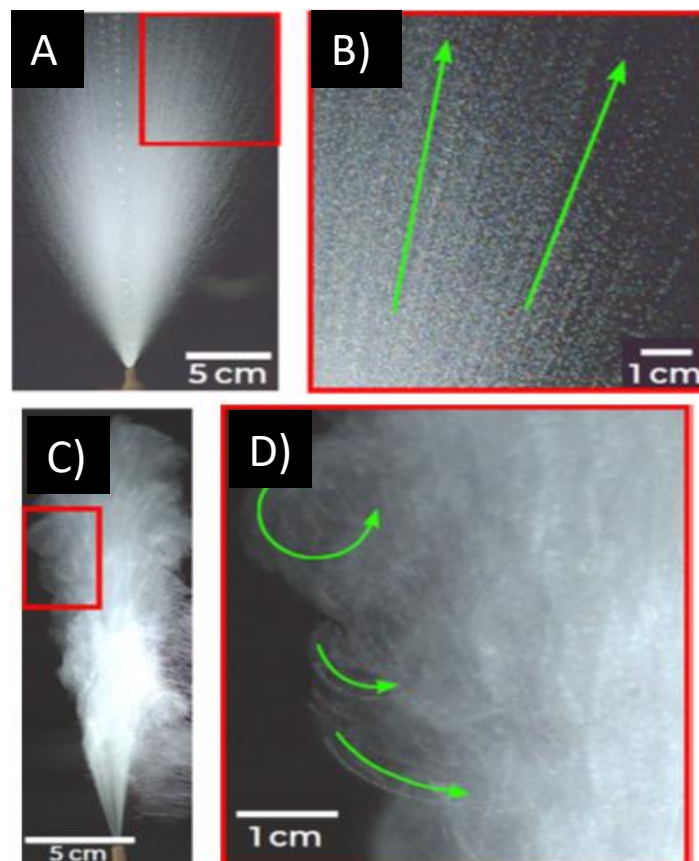

Figure 5: *Displaying the characteristics of the plume and jet of the soft mist and swirl nozzle. A Shows the soft mist nozzle spray, with B a zoomed-in shot that shows the behaviour of the plume. C shows the jet produced by the swirl nozzle, whereas D shows a zoomed-in view of the droplet behaviour.*[1]

2.4 Literature study

To acquire information regarding the best-fitting approach for the quantification of deposition from nasal sprays a literature review was performed. Google Scholar, Scopus, and PubMed were used to search for related articles regarding nasal sprays. Following this research, methods to analyse the results were gathered. Each method was further investigated to understand the working principle and requirements to quantify deposition patterns. The literature study will explore models used to examine nasal deposition patterns. Secondly, it will examine techniques that can be applied to those models. Finally, materials are required to perform these techniques. These three elements are the main elements to create a quantification analysis, this section will study them separately. Here advantages and disadvantages will be established, which will lead to the best method to perform experiments to quantify the dispersal of nasal spray in the nasal cavity. The following keywords and a combination of these keywords were used to search for literature:

- Nasal cast
- Aerosol deposition
- Quantification
- 3D printing
- Koken nasal cast
- Optinose cast
- Alberta idealized nasal inlet
- Computational fluid dynamics
- Scintigraphy
- Spectroscopy
- Photo analysis
- Radioactive labelling
- Water finding paste
- Food dye
- Visual spectrum dye
- Fluorescent dye

2.4.1 Introduction Models, Analysis Methods, and Materials

The field of nasal research has expanded in the use of models, analysis methods and materials. The literature study was designed to find the best combination between these three areas. The models that are investigated in this paper are 3D printed models, the Koken nasal cast, the Optinose nasal cast, and the Alberta Idealized Nasal Inlet (AINI). For analysis methods, computational fluid dynamics, scintigraphy, spectroscopy, and photo analysis were investigated. When exploring materials the main criteria for inclusion was to be able to work with one of the analysis methods. Therefore, the list consists of radioactive labelling, water-finding paste, Visual spectrum dye, and fluorescent dye. In the following chapters, each will be explored with limitations and advantages that allow this study to find the most suitable combination to perform quantification.

2.4.2 Nasal models

2.4.2.1 3D printed model

The first in vitro models that were used were cadavers. However, tissue retraction and preservation limited the use of cadaver models significantly. To overcome these limitations a process to replace water and lipids with silicon was used to create a silicon cast, which resulted in an anatomical representative model that could be preserved.[42] However, this is still an intensive practice. With the upcoming imaging technology such as CT scanning, creating extensive 3D digital models became possible. Computer-aided design (CAD) models were made from these CT scans with the limitation of resolution being determined by the slice thickness.[43]
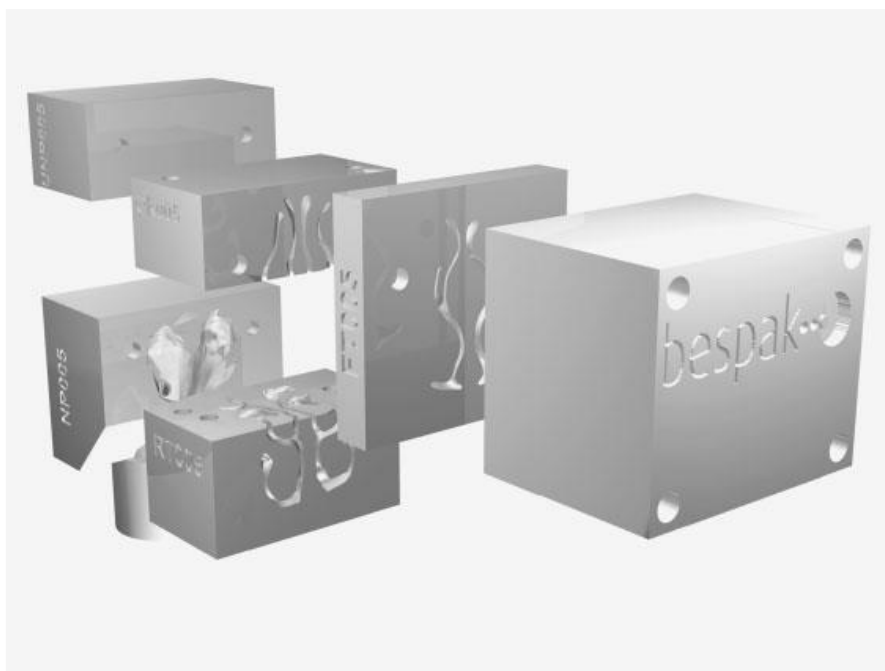
Figure 6: Nasal model CAD representation[43]

Traditional manufacturing was found to be a detriment to the complexity of the geometry. With the introduction of rapid prototyping (RP) and rapid manufacturing (RM), it became possible to transfer these digital models to physical models.[43] With 3D printers becoming more accessible, researchers could create these models locally. It allowed researchers to have a wide range of possible models to examine as nasal anatomy varies greatly between individuals.[43] Even when creating a standardized model this will lead to many challenges, with 3D modelling software averages can be established. However, defects and anatomical changes over time need to be considered in the model.[44] A researcher created a model that divided the nasal cast into its separate regions, namely the nasal vestibule, respiratory region, and olfactory region respectively. This allowed the researchers to analyse each region separately. However, in this model, adequate sealing between regions was necessary to prevent leakage. [45]

The choice of material is very important when creating a nasal cast. Current technology 3D printers have a wide range of available substances it can print. However, different materials require different printing techniques and not all printers can print all materials. The main types of printers are stereolithography (SLA), selective laser sintering (SLS), and fused deposition modelling (FDM).[46] PLA which is used in most home printers is printed using FDM. However, this material is porous, which

will absorb the nasal spray. This absorption is not representative of real-life absorption factors and creates problems while trying to clean the model, therefore, not suitable as printing material. There are also powder materials that can form a solid plastic model. One example is Duraform Pa. This material can be sterilized.[43] An alternative to PLA is also resin printers that use the SLS printing method, which allows 3D printers to print a silicon cast.[46] This material is not porous which allows for easy cleaning. Due to the nature of these materials, the ciliary clearance of the nose cannot currently be simulated in models as the material is stationary. Mucosal absorption can be recreated by applying a coating to the printed material.[43]

2.4.2.2 Koken nasal cast

The Koken nasal cast is widely used for educational and commercial research purposes.[47] This model is made from a silicon cast that is based on the scans retrieved from an Asian female cadaver.[22] It can be split into two halves and has a flat septum. The transparent septum is removable for better visualization. The main purpose of this model is to enable people insight into nasal anatomy. [42] However, due to being commercially available, multiple studies use it to visualize deposition patterns.[1,48–50] This model simulates many of the anatomical complex nasal structures, such as the turbinate area. However, having a flat septum does influence the airflow through the model. Additionally, the model was based on the scans of a cadaver, which caused more space in the cavity of the nose. Which has an additional effect on deposition patterns.[22] The volume of nasal cavities is controlled by the turbinates and varies not only between people but can change due to humidity and temperature.[3]

One of the benefits that contribute to the model's effectiveness is the material it is made of. The silicon allows for rapid screening as it is easy to prepare for use and cleaning.[42] Keeping the workload of using this specific model very low. As this model is transparent it allows researchers to quickly inspect the result through visual inspection before implementing more extensive analysis methods.[1]

The model has two pieces, which allows for one nasal cavity to be examined at once. However, the nasal cast is not dividable physically in the different regions of the nose. With medication that targets the brain, or specific regions of the nasal cavity it's important to understand the deposition pattern. With this model when examining quantification methods, it will be important to create a digital region division, that allows for greater inspection of deposition patterns. Important to realize that physical region divisions have a higher accuracy as digital is more prone to user error in the placement of the camera and model.[1] A method of physical washout needed for spectroscopy can be created; however, it will be important to allow for reproducibility. For instance, partial submersion can allow for targeted washout but has a high possibility for errors due to the dripping of the solvent. Also, submersion does not allow specific regions to be investigated due to the nature of the method. This is due to the 3D nature of the model. As with all silicon models, there is no mucociliary clearance.[43] Even when applying a layer to simulate the mucosal layer, the clearance cannot be simulated in this model as it will be a stationary layer. While this will still allow for initial deposition analysis, it's important to realize the difference between the model and real-life situations. Finally, there is a high level of anatomical variations in humans.[17] With a singular commercial model that is based on a singular individual, this variation is not considered. Combined with the fact that the scans are from a cadaver, which causes the nasal cavities to be wider than found in living human beings.[22]

Figure 7: The Koken nasal cast[47]

2.4.2.3 Optinose

The nasal cast used by Optinose was intended to be an accurate reproduction of human intranasal geometry and dimensions. In the development of this cast 3D computer reconstruction and surface rendering from a high-resolution MRI in a non-decongested, healthy, 26-year-old male.[22] To create a model close to the usage of their exhalation delivery device, namely the Optinose AS, the subject was asked to exhale through the mouth against resistance. This manoeuvre is an airtight seal of the velum separating the oral and nasal cavities.[51] Additionally, for this cast, through a computer-aided design program, the two nasal cavities were parallel shifted by 8 mm to be able to split the septum into two parts with sufficient thickness and rigidity to maintain the septum internal geometry while not changing the internal geometry of the nasal cavities on either side.[22] To allow for the two halves to maintain normal communication, this was also extended by 8 mm. Which is located behind the posterior margin of the nasal septum. During the MRI the upper narrow section of the nasal valve was naturally partly collapsed and occluded by normal secretions.[22] Which is frequently the case in rest and inspiration. To maintain a fluid and dynamic pathway that allows realistic valve behaviour, the two walls of the valve were separated slightly in the computer-aided design model. While this adaptation causes deviation from the in vivo dimensions of the valve as measured by acoustic rhinometry, it is representative of the situation during the insertion of the Optinose EDS nosepiece, during exhalation delivery, and during nasal exhalation. From the digitally acquired model, a detailed replica was printed using a stereolithographic 3D printer. Subsequently, this geometry was placed in a box filled with fluid, semi-transparent, semi-soft silicone. After drying the cast was broken into its separate pieces. The finalized model can be seen in Figure 8.[22]
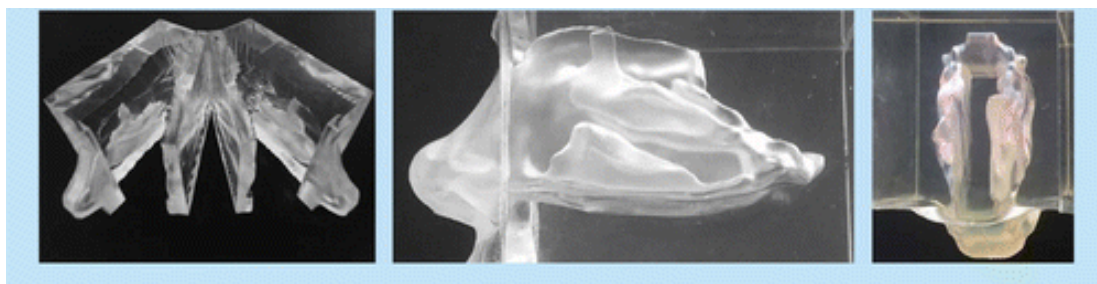

Figure 8: Finalized model of the Optinose Nasal Cast[22]

The main advantage of the Optinose nasal model, especially when compared to the Koken model, is that it is based on a living human. Which have the nasal cavities that represent the anatomy closer to living models. Due to their smaller sizes in this model. The effect of this is that deposition patterns found in this model are closer to in vivo circumstances. A comparison study of the two models found that when compared to 30 living subjects the Optinose showed a more representable image of the nasal cavity.[22] The similar characteristics will lead to the same other advantages the Koken nasal cast has, such as allowing for rapid screening and easy visualization.

However, that will cause similar disadvantages as well. The model is created as two halves that represent the two nasal cavities. There is a version that is divided into four sectors which allow for medial and lateral aspects of the cavity. It will still not be sufficient to allow for accurate and reproducible washout of different regions in the nasal cavity. Finally, this model is currently not commercially available.[22] Thus, while establishing that the Koken model can be vastly improved upon, based on anatomical accuracy, it is not an available alternative for this research to implement this model.

2.4.2.4 AINI

Whereas Koken and Optinose chose realistic geometries to base their models on, University of Alberta together with Copley Scientific created an idealized computational model to create a physical model. Initially developed to reduce the computational time that was found using realistic models as it reduced the complexity of the geometry of the nasal region.[52] To create an idealized geometry, first, the CT scans from healthy subjects were collected. The ages of the subjects ranged from 27 to 73 years old acquired from 7 males and 3 females. The scans extended to below the larynx region. Each nasal geometry has 2 independent and proximal airway paths, as for one for each nostril, which provided a total of 20 scans to be used in the creation of the idealized geometry.[52,53] By applying averaging, smoothing, and simplifying techniques the complex geometries were reduced to a single idealistic computer model.

The first version of the real-world model was made from plastic to test its viability, however, due to the limitation of the plastic construction of the geometry only water was suitable as a solvent for extracting deposited from the geometry surface, and thus only a single nasal spray product was tested. As a further development, the Alberta Idealized Nasal Inlet (AINI; Copley Scientific, UK) was developed.[53] This is an aluminium version as can be seen in Figure 4 [25]. AINI consists of 5 separate elements that allow for several regions to be washed out and analysed. These regions represent the nasal vestibule, respiratory region, olfactory region, and nasopharynx. The AINI model can easily be attached with cascade impactors if necessary. Each region can be separately analysed using techniques that can analyse washouts from models.

As with most models, this model is a stationary version of a nasal cavity, therefor there is no mucociliary clearance.[53] However, unlike 3D printed-, the Koken or the Optinose model it is not possible to apply a coating to simulate mucociliary clearance. Additionally, this model does not have nostrils, these anatomical structures aid in controlling airflow and aid in the filtration function as the first part of the nasal vestibule.[53] Especially in the case of the soft mist nozzle, this specific absence of the nostrils has a very significant impact on performance, as the soft mist droplets are more likely to follow the airstreams. This will affect simulating nasal spray behaviour as in daily practice the nozzle is inserted into the anterior nares. As this model is made of aluminium it is not possible to apply

rapid visual screening techniques to this model. This increases the workload to work with this model and at the cost of around 15000, this is one of the more expensive models. Finally, an idealized model simplifies complex geometries, which produces an approximation of a realistic model.[52]

2.4.2.5 Summary

The difference between the 3D-printed model, the Koken model, and the Optinose model is the model they are based on. From the literature study, the Optinose model did prove to be more accurate than the Koken model however due to the model not being commercially available. It is not possible to substitute the Koken model for the Optinose model. It did highlight the disadvantages of the Koken model, which would impact further studies in correlating in vitro data compared to in vivo data that has been acquired. 3D-printed models can prove useful in the future. As it can allow for multiple models to be created. This will introduce the additional step to validate the model. Therefore, developing the quantification method on an already widely investigated model to explore the approach can be beneficial, before implementing a new anatomical model. The AINI model is based upon an entirely different principle, following the path to create an idealized model instead of realistic geometries. Additionally, visual techniques are not possible with this model, which limits the possible methods that can be applied to the model.

With future developments in model creation and looking at the found advantages and disadvantages as shown in Table 1. This study concludes that preliminary research is best conducted with the Koken model. Due to its easy availability and rapid screening possibilities allows for the testing of new methodologies very easily. As well as using the developed methodology using the Koken model can be easily transferred to a new model using the same material but with different geometry. Thus, allowing for the development of a method that can be applied to different anatomical situations.

Table 1: Summary of the attributes of the different models

Model	3D-print	Koken nasal cast	Optinose nasal cast	AINI
Properties	- Self-printed model using CFD models. - Can be made everywhere there is an adequate printer	- Model based on a cadaver scan from an Asian woman. - Made using silicon resin. - Originally made for educational visualization of the nasal region.	- The model is based on a 26-year-old Caucasian male. - Made using Silicon resin. - Designed for internal testing by Optinose.	- Made from aluminium. - The first part simulates the nasal area, the second part the Nasopharynx, third part lungs. Can easily be connected with a cascade impactor.
Requirements	- Material to visualize distribution (coating or formulation) - Printer, Digital model, and filament	- Material to visualize distribution (coating or formulation)	- Material to visualize distribution (coating or formulation)	- Compartment washout. - Analysed by tools such as spectroscopy.
Advantages	- Self-manufacturing - Commercially available (except for CAD models) - Custom regions - Visual representation - Viable for many methods - Rapid screening	- Commercially available - Much research was performed with this model. - Visual representation - Viable for many methods - Rapid screening	- Due to a living human used for scanning higher accuracy of spacing in cavities. - Visual representation - Viable for many methods	- Each region can be separately removed and washed out allowing for easy spectroscopy. - The AINI can be used without the impactor by replacing it with a filter reducing the potential workload
Limitations	- Sealing necessary - PLA porous material therefore right material is required for coating. - No mucociliary clearance - Many anatomical variations	- No region washout possibilities - Based on a single model - No mucociliary clearance - Airtight sealing is needed. - Not taking anatomical variation into account - Due to the cadaver scan bigger nasal cavities	- Not commercially available - Airtight sealing is needed. - No mucociliary clearance - Based on a single person therefore not taking anatomical variation into account	- Unable to have a Visual inspection of the spray. - No mucociliary clearance - No nostrils, which greatly affect the performance of soft mist sprays.
Cost/workload	- Printing time Printer around $170,000.00 - High initial workload due to printing requirements.	- Between 800 and 1200 euros - Delivery time 4 weeks - Medium workload due to cleaning requirements	N/A	- 15.000 euro - High workload

2.4.3 Analysis methods

2.4.3.1 Computational fluid dynamics

The models are created by using digital models and translating them into physical products. However, computational fluid dynamics (CFD) can directly use the digital model to create simulations of deposition patterns.[54] By creating mathematical models to predict the behaviour of airflow and particle distribution. By applying more complex mathematical models to simulate the behaviour the fluid flow can be better predicted.[55]

To simulate these models, software such as SolidWorks can apply the mathematical models to complex geometric models to illustrate the fluid behaviour. The more complex the model the higher the accuracy of the prediction simulation.[55] However, this will also increase the computational requirements of the simulation. An approach to reduce the computational load is to simplify the model resulting in idealistic models that can mimic realistic models accurately.[53] Due to these models lacking the unconnected structural changes found in realistic anatomical models, calculations become easier to perform. However, this will create an additional validation step to assess the CFD model for real-world circumstances.[53] Therefore, it is important that in the creation of the digital model, accuracy and computational time are weighed in balance to desired outcomes in a matter of precision. Both the resolution of the fluid and time length are the other two factors that impact computational time. Where to simulate the behaviour of singular droplets can cause simulations to need hours of computational time.[55]

2.4.3.2 Scintigraphy

Scintigraphy is a nuclear imaging technique that visualizes the internal physiological processes and functions within the human body. At the heart of the scintigraphy lies the use of radioactive labels. The radioactive labels are isotopes that emit gamma radiation.[56]

A specialized camera known as a scintillation camera or gamma camera is employed to detect the gamma rays emitted by the radioactive label. This gamma camera consists of a scintillation crystal coupled to photomultiplier tubes or other light-sensitive detectors. When a gamma ray interacts with the crystal, it generates flashes of light (scintillations), which are then converted into electrical signals for further processing.[57]

The information acquired can be used to quantify aerosol deposition when the radioactive label is applied. This will allow not only for dispersal patterns to be made visible but quantity and time-based analysis.[58] Additionally, this functional imaging technique can be used to observe absorption which could allow for future analysis on medicinal absorption.[56]

However, this technique has a lower spatial resolution compared to other imaging techniques, which possibly can make it hard to differentiate in the complex nasal geometry for aerosol dispersal patterns.[58] This results in a decreased anatomical detail for visual inspection. Additionally, this technique relies on the usage of radioactive tracers, therefore, limiting the usage of a wider variety of formulations that can be used.

2.4.3.3 Spectroscopy

Substances have an absorption spectrum at which energy is absorbed. Spectroscopy uses this interaction of light and matter to analyse the composition, physical structure, and electronic structure of matter on an atomic, molecular, and macro scale. Each substance has its own absorption

and excitation peaks. By analysing these graphs, it can be possible to determine the concentration and quantity of substances. For instance, using the ultraviolet-visible light spectrum the transmittance, reflectance, and photoluminescence can be used to investigate solutions.[59]

This is performed by having energy in that spectrum penetrate the substance and detect reflection, absorption, and transmittance. As every molecule has a different absorption and excitation spectrum it can differentiate the molecules that are reactive in this spectrum. As energy enters the substance the energy is absorbed, transmitted, and reflected. This can be detected using a detector, which can then calculate the concentration of the reactive substance. [59,60]

Spectroscopy can be applied to many formulations, allowing researchers to examine different drugs. The importance is that the formulation has a reactive component in the analysed spectrum. With non-reactive formulations, it will be necessary to add a reactive component to quantify the deposition of the aerosol. Which can be quantified with a high accuracy in the composition of the substance.[61]

However, any alteration to the path of the energy can change the results. Research that applies this technique often uses washout methods to collect and analyse the aerosol deposition. Using models like AINI it is possible to wash out specific regions.[14] With 3D models such as Koken and Optinose models, this is not possible due to the complex geometric shape and reproducibility with accuracy. It is possible to perform spectroscopy without washing out the model by placing the energy source and detector around these transparent models. The problem that arises then is that the model also affects how the energy is transported through the model, which reduces the accuracy of the analysis.[22] Additionally, if the spectra of the substances in a formulation have similar absorption and excitation properties it can be difficult to differentiate. Therefore, it is important to create formulations that have little to no overlap in these spectra to achieve the accuracy desired for quantification.

This will increase the workload when analysing using this technique. After application, the aerosol deposition will be needed to wash out of the model and placed in a spectroscopy analysis device. Adding additional steps to acquire the data for quantification.

2.4.3.4 Photo analysis

By using image analysis software, it is possible to examine differences in the image. For instance, a colour gradient can be found and analysed.[14] When using materials that create a change in the nasal cast, this method can then be used to quantify these changes. Sensitivity and specificity are determined by the equipment used to acquire the image. With the main factors being camera resolution and background interference. These acquired images can then be loaded into programs such as Photoshop or ImageJ. The software allows for manually applying filters and analysis of the intensity. Programs such as Python allow for the automatization of these processes.

However, before automatization is possible, it is required to determine the adequate settings of filters to highlight the image in regions that provide data in the desired spectra. Applying this analysis technique, it is possible to quantify a visual representation of the aerosol deposition. Allowing for rapid screening to observe changes due to aerosol deposition.[1]

This approach does require a visible alteration due to aerosol deposition, which causes a limitation in formulations that can be applied to this model. Either a dye that changes colour or a fluorescence is

required to analyse the data. Additionally, initial imagery is a 2d representation from a complex 3D representation. Therefore, it is important to calibrate the acquired data to achieve accuracy and perform validation studies.

2.4.3.5 Summary

While each method can be used to quantify aerosol dispersal, this study examines the limitations of each to determine the best possible approach. While CFD has the advantages of being a digital model, computational time and resulting resolution limit its current possibilities to analyse complex droplet behaviour between two different nasal sprays within a great enough time frame. Whereas scintigraphy has a reduced spatial image resolution and increased safety procedures which cause it to be an intensive specialized method to analyse the quantification of aerosol deposition. While spectroscopy has excellent accuracy, it requires to be precisely washed out of the model for accurate readings. This entails that either a model is used that can be separated, or a model that can be washed out precisely every usage. Which would incorporate losing the capability of visual inspection using the AINI model or adapting a model for accurate analysis. With photo analysis, this will not be necessary as accurate division of regions can be created using the software and therefore have a greater range of models that can be applied to this method. This makes photo analysis an interesting method to develop quantification for aerosol deposition, which additionally allows for rapid screening of visual information as summarized in Table 2.

Table 2: Summary of the attributes of the different analysis methods

Analysis method	CFD	Scintigraphy	Spectroscopy	Photo analysis
Principle	- Using mathematical models to create simulations that estimate the behaviour of fluid	- Utilizing gamma radiation to generate a three-dimensional map of anatomical structures and analysing the detected energy	- Using absorption and emission rates of substances at different energies this technique calculates concentration.	- Using photo analysis software this method detects changes in colour to detect the quantity
Requirements	- Software (SolidWorks, Ansys, Python) - Digital Nasal model	- Scintigraph - Analysis software	- Energy source - Detector - Reactive substance	- Camera - Photo analysis software
Advantages	- Detailed digital model - Adaptation is possible for individuals	- 3D analysis - Both in vivo and in vitro are possible. - Individual anatomy differentiation - Visual representation	- High accuracy - Wider formulation range - Differentiate between concentration and quantity.	- Visual inspection - Rapid screening - Not formulation dependant (just need contrasting)
Limitations	- Only simulates fluid dynamics, not particle interaction. - Models need calibration and validation using real-life models.	- Requires radioactive isotopes or contrast material to highlight deposition. - Requires CT tomography which is not easily accessible. - Long scanning time Slicing of images affects the accuracy	- Washout needed from the model. - If using a laser on the model diffraction caused by the 3D model may cause a heightened result	- Concentration dependant - Coating dependant - Manual setup
Cost/workload	- The programs used range from free to subscription fees for software. - Long computational time	- High costs due to requiring specialised lab needed. - High workload	- Around 2000 dollars for UV-VIS spectroscopy - Medium workload	- Camera around 500-1000 euros - Software: Free to 27 euros/month - Workload low with automatization.

2.4.4 Materials

2.4.4.1 Radioactive labelling

Using a technique that can measure radioactive decay, this activity can be used to quantify aerosol deposition. However, to achieve this a radioactive tracer needs to be added to the formulation. Substances like carbon-14 (14C labelling), tritium (3H), and sulfur-35 (35S) can be added to formulations to use their radioactive decay to quantify aerosol deposition. By measuring the intensity of the radioactive emission, it is possible to determine the quantity of the formulation.

The activity can be collected using scintigraphy and translated into a map of quantity tied to intensity. This time-based analysis has a high accuracy in determining quantity.[56] This is because the technology tracks the path of the particle showing where it has been and ended up. As specialized imaging equipment can visualize the activity this can be correlated to the quantity and concentration of the formulation that the isotope is added to, which allows this tracking to occur.[58]

However, due to the nature of radioactive isotopes, strict safety protocols need to be followed to use this material. Which severely increases workload and prevents rapid screening of the aerosol deposition. Additionally creating radioactive isotopes is a time-consuming and expensive procedure which increases the cost of the testing method for quantification.

2.4.4.2 Water finding paste

A way to detect changes in a model is to introduce a substance that will change colour based on contact. Water-finding pastes is a gel that when in contact with water will change colour.[1] For instance, Sar-Gel is a water-finding paste that changes from white to purple in contact with water. An alternative to Sar-Gel is Kolor-Kut, which changes from yellow to deep red respectively. It allows for visualization of the deposition patterns in the nasal cast, as is shown in Figure 2.[1]

This material can be used in conjunction with photo-analysis to determine the quantity of deposition. Current research has used this technique to visualize the regions that aerosol deposition coats.[14] While hypothesized that it is possible to determine the volume of the deposition some limitations impact the accuracy of this approach. Namely, the coating thickness of the applied water-finding paste affects the colour-changing reaction to liquids.[1] Unlike the other materials, this material is less dependent on the formulation of the aerosol, with the only requirement being that is based on water.

A tube of water-finding paste costs around 8 euros for 30 ml, which is sufficient to coat a model multiple times. However, while not expensive there is a significant increase in workload. As stated, coating thickness affects accuracy therefore, it is important to apply the gel evenly throughout the model. As the model is a complex geometric shape this can prove not only a tedious task but also effecting the reproducibility of the experiments.[1]

2.4.4.3 Visual colour dye

Applying the principle of water-finding paste, of affecting a colour change in the aerosol deposition, to the formulation instead of the model.[14] To achieve this, a drug-grade food colouring can be added to the formulation before deposition. This will create a colouring of the model, which can then be analysed through photo-analysis and spectroscopy.[62] Examples of substances that qualify are Tartrazine yellow, brilliant blue FCF, and Allura red. Each of these dyes has excellent solubility in

water, with tartrazine yellow 20mg/100ml of water.[63] Allowing the approach to be used in a nasal spray.

The concentration of the dye will affect the colour that can be seen from the deposition of the aerosol. Two variables affect the colour of the deposition. Namely, the concentration and quantity of the food dye.[64] This study hypothesizes that with a fixed concentration the colour differences can be tied to the quantity of the aerosol. Which can be used for volume calculations. As these dyes do not rely on external sources to display colour, they will not require special light sources.

Although no special light sources are required, uniform lighting is needed for the model. External light sources can cause colour shifts. Therefore, to achieve accuracy it might be required to create a controlled environment, where uniform lighting can be achieved. Background effect which can cause additional shadows. These shadows can cause differences in colour tone as the dye itself does not provide detectable energy at a certain wavelength. [65]

The cost of the food dye is around 7 euros for 25 grams. At this time, it is unknown in what quantities are needed to have a concentration that shows a visible scale that can be tied to quantity. With 70 ml per actuation, each spray has a maximum concentration of 14 mg/70ml. Additional experiments will be required to develop a quantification method to determine the colour shift with volumes. For workload, this will require the food dye to be added to the formulation in preparation for the experiments.

2.4.4.4 Fluorescent dye

Another method to create a visual representation of dispersal is by adding fluorescent dye to a solution. These dyes have a specific absorption and emission spectrum at which a certain frequency of light is emitted. For instance, Calcein is a soluble fluorescent dye (10mg/100ml) that has an absorption/emission spectrum of 491/511 nm respectively.[1] The higher the concentration the less energy is required to cause the fluorescence to emit light. These energies can be detected and allow for mathematical calculations in concentrations or quantities.

However, to acquire this information a specialized setup is required that mitigates background interference. A dark box can be created to house a singular light source that emits constant energy into the system, allowing for optimal detection of fluorescence. Current studies aim to find a high emission of the fluorescent dye, which allows for quantification of the aerosol coverage.[1,61,66]

Like the visual spectrum dye, this material is not dependent on a coating layer of the model. Additionally, this technique will reduce the influence of external interference due to the fluorescence reacting with specific energy bands. To acquire optimal results a controlled environment such as the mentioned dark box will be needed.[1]

Calibration to find the right formulation and concentration will be required to establish the optimal emission response to determine quantity. For quantification a concentration needs to be found that can differentiate between different volumes to establish the quantity of aerosol deposition.

2.4.4.5 Summary

The selection of materials is dependent on the selection of the model and analysis method. Radioactive labelling requires CT or scintigraphy to collect the radioactive decay that can quantify the deposition. Whereas water-finding gel requires a visual inspection tool such as photo analysis. Dye that alters the colour of formulation in the visual spectrum can be analysed using both spectroscopy and a photo analysis method. However, compared to fluorescence, visual spectrum dye has a wider range of response, and its colour is more influenced by external factors. In combination with the Koken model and photo analysis, a fluorescent dye is a suitable candidate for analysis, as shown in Table 3. With a controlled environment and specific absorption and emission spectra, it will enable accurate material analysis. Additionally, this material is also suitable for spectroscopy, which might serve as a backup approach if photo analysis does not provide the required accuracy for suitable quantification.

Table 3: Summary of the attributes of the different materials

Materials	Radioactive Labelling	Water finding paste	Visual spectrum dye	Fluorescent dye
Properties	- Substances like carbon-14 (14C labelling), tritium (3H), and sulfur-35 (35S). - These materials give off radioactive energy which can be detected through scintigraphy or CT scanner.	- A paste that changes water when in contact with fluids.	- The dyes that can colour solutions (Tartrazine, brilliant blue FCF, Allura red)	- Dyes that are fluorescent with proper excitation (calcein, rhodamine 590, tryptophan)
Requirements	- Radioactive Tracer added to the solution. - Detector - User safe environment	- Dehumidified room - Water - Equally applied across the model	- Addition to a formulation that causes the deposition to colour the model. - Capture device	- Addition to a formulation that reacts to certain light frequencies. - Light source - Darkbox - Capture device
Advantages	- Radioactivity directly tied to concentration. - Detectable through materials	- Not formulation dependent - Not dependent on an external light source	- No need specific light frequency - Less impact environmental effects compared to a fluorescent dye.	- Not dependant on a coating of model - Specific reaction to certain light frequencies
Limitations	- Requires specific equipment for detection. - Activity is time-based, which causes quantity analysis to take time into account.	Calibration required. Hard to apply equally. Sensitivity/specificity	- Calibration needed. - Concentration dependant - Background effect - Need uniform lighting.	- Calibration needed. - Need specific lighting at specific frequencies. - Requires specific solution. - Sensitivity/specificity
Cost/workload	- 25.000 euros per 800 mg	- 8 dollars per tube	- 7 euros per 25 gram	- 85 euros per 100 mg

3 Methods

3.1 Materials

The fluorescent compound calcein (C30H¬26N2O13¬) obtained from Carl Roth, Karlsruhe, Germany, with a molecular weight (MW) of 622.55 g/mol, was utilized in the study. During the calibration phase, various concentrations of calcein ranging from 0.2 mg/ml to 0.8 mg/ml were analysed. To maintain fluorescence stability over time, glycerol was introduced into the solution, resulting in an aqueous solution comprising 25% glycerol, exhibiting viscosities between 2 and 10 cP.

A Velleman® UV Lamp (ZLUVB, Velleman NV, Gavere, Belgium) was employed as the UV radiation source, emitting rays with a wavelength of 366 nm to induce calcein emission. To mitigate background interference, the lamp was enclosed within a sealable dark box. Image capture was facilitated using a Nikon D3400 camera equipped with 24.2 megapixels and a lens aperture of 18-105mm, set to an 18mm focal length and a focal point (f) of 5.6. The exposure time was set to one-fifth of a second, with an ISO of 3200. The complete experimental setup is illustrated in Figure 10.

Figure 9: Setup inside the dark box for acquiring images of calcein deposition.

3.2 Experiments

The experiments are divided into multiple groups. The first experiments will focus on developing the method to quantify a liquid based on the intensity of the fluorescent dye. The experiments will be analysed using the method described in <u>section 3.3</u>.

3.2.1 Calibration

The first step was calibration. In a study conducted by Yano, Hamada, and Amagai et al, the thickness of a solution can be directly correlated to the intensity[67]. Figure 10 shows the container's measurements. With a total length of 80 mm and 40 mm wide, the plates are connected using glue that is not UV-reactive. Using a spacer of 2.4 mm thick and 3 mm wide, an angle of 1.77 degrees is created to allow for thickness variance. The resulting container is shown in Figure 11. This container was filled with the solution with the fluorescent dye to calibrate the algorithm for quantification. This container was initially placed 13 cm from the camera lens. This distance is the equivalent of the centre of the Koken model placement. Using this initial placement calibration curves can be created. Using the pixel intensities with their placement to calculate a trendline that can determine the thickness connected to each intensity value.
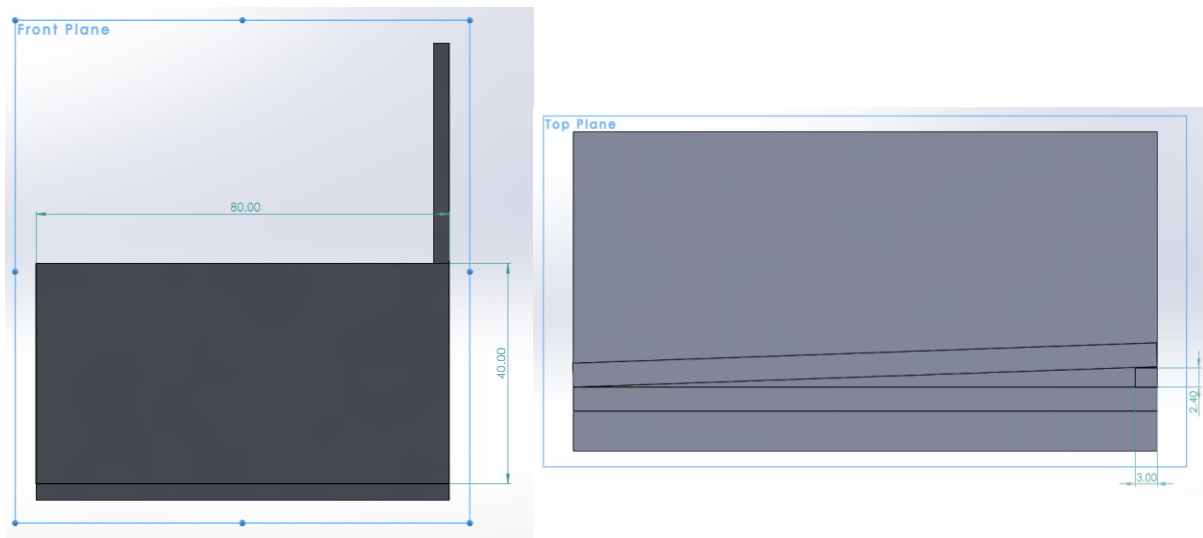
Figure 10: Schematics of the calibration container, where left shows the front and right the top view
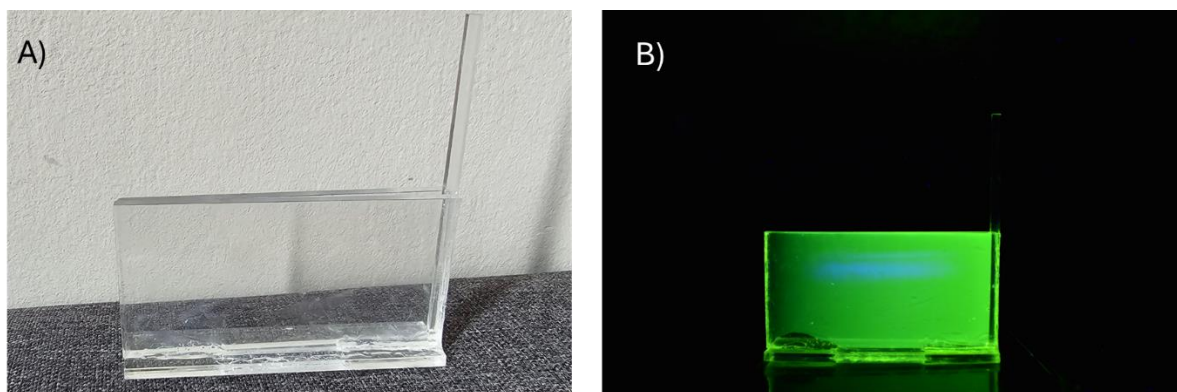
Figure 11: The constructed calibration container. A shows the empty container, whereas B displays the container in the dark box under UV Light filled with 0.2 mg/ml Calcein

3.2.2 Colour intensity

When performing photo analysis, it is important to understand how digital systems currently process colour differences. To determine colour shifts in systems such as described in 2.4.3.4, intensity coding can be divided into the three primary colours of light: Red, Green, and Blue (RGB). Each variable is encoded in an 8-bit system, which allows for 256 values to be stored per channel. This creates a range from 0 (no contribution of that colour) to 255 (maximum contribution), for example, green is represented as (0, 255, 0), where the red and blue channels are zero, and the green channel is at its maximum intensity. Although current systems could allow for more extensive colour coding by using 16-bit or higher encoding, it was determined that the increase in memory usage was detrimental to algorithm performance. Additionally, most image processing systems have incorporated this colour coding system, allowing this study to not be dependent on specific programs and equipment for colour acquisition. This will give this study 256 levels of intensity to explore and correlate to depth.[68]

3.2.3 Verification

Several variables will be investigated to verify if the correct analysis is being performed. First, the concentration of calcein will be determined to be suitable for the quantification of aerosol deposition. In this study, the choice was made to test 0.2 mg/ml, 0.4 mg/ml, and 0.8 mg/ml. From these, the range in intensity can be observed, which will allow this study to select the correct concentration for the desired resolution in different thicknesses of deposition.

The distance to the camera and UV light will be explored as a second parameter. The maximum thickness in the Koken model is around 1 cm deep. Therefore, an experiment will be conducted with the same formulation in the container. However, the distance of the container will increase with steps of 1 mm to examine the effect this range of distance will have on the quantification method. The starting distance from the camera lens is 13 cm which is the centre of where the Koken model will be situated.

The layer thickness of the plexiglass will be increased to explore the effect of the extra distance the UV light has to travel and the emitted photons from the fluorescence back to the camera. This will allow the investigation to be aware of variables that can affect the accuracy of the analysis.

The final variable that will be investigated through an experiment will be the effect of multiple layers of calcein deposition. By placing a microcuvette behind the container at multiple places the enhancing effect of multiple layers can be explored.

3.2.4 Validation

From the verification method, a calibration curve will be established. This calibration curve for thickness will be validated by applying a known quantity to the flat surface of the Koken nasal cast. Afterwards to establish the effect of deposition in a 3D model has on quantification. This allows for the investigation of which variables affect the photo analysis.

3.2.4.1 Flat Surface Analysis

By applying a known quantity to the flat surface of the Koken model, a simplistic quantification experiment can be conducted. By creating images as can be seen in addendum B.1.1, factors such as distance and angles will be limited due to the flat surface. By analysing the acquired image using the calibration curve a quantity can be derived. Comparing this to the known quantity achieved by weighing the syringe before and after application, accuracy can be determined in testing the validity of this method of aerosol deposition. The deposition will be created by manual application with a syringe that has a soft mist nozzle attached to it, which will be referred to as a soft mist atomizer.

3.2.4.2 Koken Model Analysis

When the quantification algorithm is functional in analysing flat surfaces, the same algorithm will be tested using the nasal cavity of the Koken Nasal cast. The soft mist atomizer is weighed before and after application and a deposition is created inside the nasal cavity. This allows for a controlled exploration of the quantification method in vivo circumstances with a limited number of parameters that influence the deposition of aerosol.

3.2.5 Quantification of aerosol deposition

Finally, the aerosol deposition of the soft mist spray will be compared to that of the standard swirl nozzle. To compare these two nozzles a testing setup up will be made in which the Koken model will be placed in the dark box. In the model, the aerosol deposition will be performed by the 4μm soft mist spray nozzle and for the standard swirl nozzle a 45ml pump will be used. Twice a deposition will be created without airflow and once with an airflow of 15L/min. The resulting images will then be analysed to determine the performance of both the quantification method of aerosol deposition and an initial comparison of the two different nasal sprays.

3.3 Analysis

The initial step of the analysis involves using a software program called ImageJ. Manual pixel locations will be determined for the boundaries of the pyramid container, compensating for any shifts in the placement of the camera and container. This information will then be fed into automated Python scripts for image analysis. The full code of the calibration algorithm is shown in Addendum A.1 and the quantification algorithm is displayed in Addendum A.2.

3.3.1 Calibration analysis

Initially, a script is developed to analyse the calibration container. The script prompts the user to load the image into the program. Once the image is selected, the user is asked to define the boundaries of the container by entering the pixel values for the upper and lower limits of the rows, as well as the left and right boundaries. Subsequently, the script transforms the image into a greyscale within the green spectrum, effectively removing background light from the UV light source. In this grayscale image, pixel values range from 0 (black) to 255 (white), where white corresponds to complete greenness. Utilising the known characteristics of the pyramid, including its width of 77.2 mm, angle of 1.77 degrees, and end thickness of 2.4 mm, the length of a single pixel is calculated. With this information, the thickness at each pixel location can be derived. Consequently, intensity and thickness at each pixel location for every row in the container are determined.

Plotting the raw intensity data against the thickness establishes a relationship between the two variables. By employing a third-order polynomial, the following formula can be derived:

$$Intensity = a * depth^3 + b * depth^2 + c * depth + d$$

Where depth is in mm, a is in mm^{-3}, b is in mm^{-2}, C is in mm^{-1} and both intensity and d are dimensionless.

Reversal of this equation allows for the calculation of thickness with the resulting intensity detected in the image loaded into the algorithm. This can be achieved by the following code in Python:

```python
a, b, c, d, _ = polynomial_coefficients_data[0]
a = float(a)
b = float(b)
c = float(c)
d = float(d)
coeffs = [a, b, c, (d - intensity)]
roots = np.roots(coeffs)
real_roots = roots[np.isreal(roots)]
real_roots = real_roots.real
valid_roots = real_roots[real_roots > 0]
```

Figure 12: Code used to calculate the depth from intensity values.

The formula and code mentioned above can be utilized to determine thickness from the 2D image obtained during the comparison between the soft mist spray and traditional swirl nozzle spray. The calibration curve will be calculated for every horizontal line in the container. To derive a singular the mean of all these lines will be calculated resulting in an average calibration equation. Averaging the fitting lines helps filter out individual artefacts and ensures a more reliable estimation of thickness.

These variables are stored in a CSV file allowing them to be loaded into another Python script to quantify the aerosol deposition. As will be shown in 4.2.1 an additional calibration was performed for the values from 0 to around 50 intensity values due to artifacts from the current calibration container. This study chooses to extrapolate the progression of the curve from 0 to the starting point of the third-order polynomial with a second-order polynomial. The resulting coefficients are stored in a separate CSV file and will be loaded separately in the quantification algorithm to manage the adequate calculation of the thickness of deposition.

3.3.2 Aerosol quantification

Like the analysis method in 3.3.1, the image will be loaded and transformed into greyscale in the green spectrum. The resulting intensities can then be inputted into the algorithm to derive the thickness of each detected pixel intensity. Using the fixed size of the model the area covered by a pixel can also be calculated as a pixel is a square. Using the following equation:

$$Area * Thickness = Volume$$

The overall volume can be derived in mm^3. This result can then be displayed with thickness intensity maps to visualize the results.

4. Results

4.1 Concentration calcein

The first step is determining which calcein concentration provides the desired resolution. At larger droplet volumes, it was established that there was minimal difference between calcein concentrations ranging from 0.2 to 0.8 mg/ml. When examining the average trendlines of the different concentrations (0.2 mg/ml, 0.4 mg/ml, and 0.8 mg/ml), as shown in Figure 13, it was found that especially at thicker layers, 0.2 mg/ml has a better resolution in distinguishing between different thicknesses. At 0.8 mg/ml, the calcein reaches maximum emission at a lower thickness, causing the blending of the layers. This effect is also observed with 0.4 mg/ml. Therefore, it was concluded that 0.2 mg/ml was the best concentration to use for quantification.
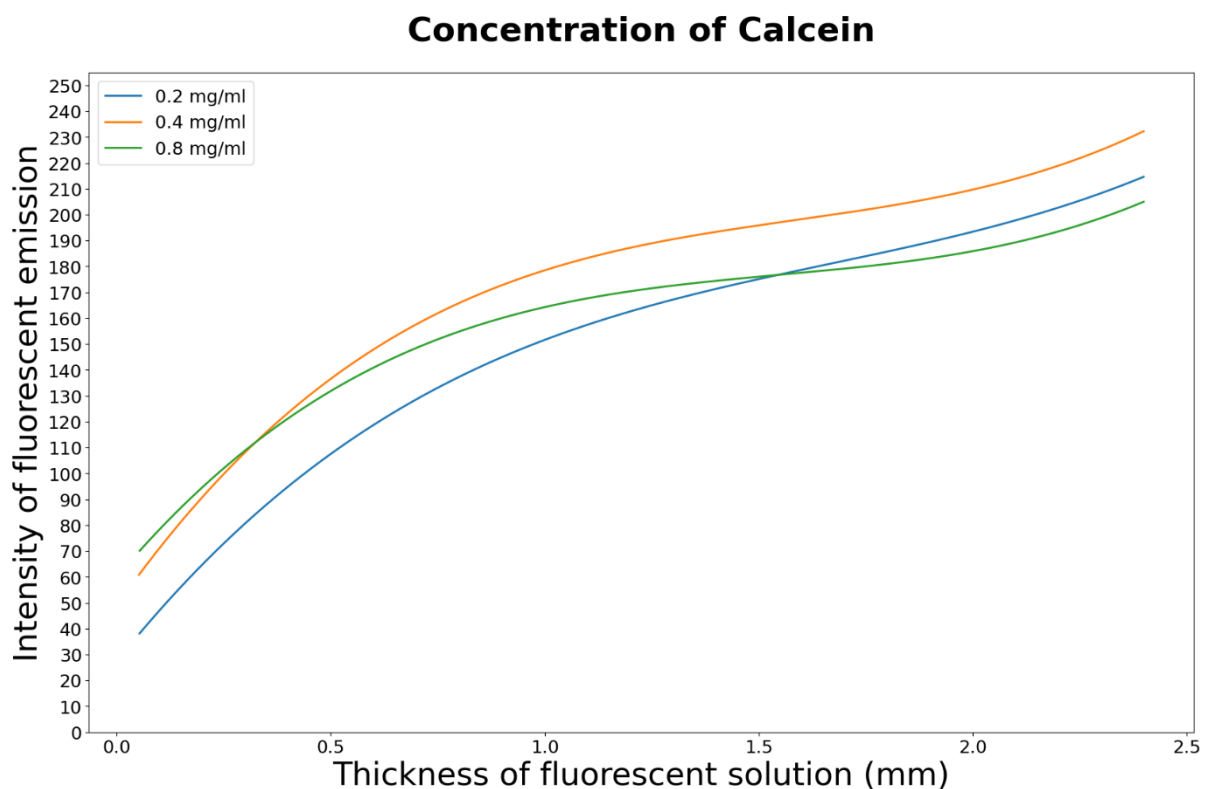
Figure 13:A plot showing the different trendlines at different calcein concentrations. blue displays 0.2 mg/ml, yellow 0.4 mg/ml, and green 0.8 mg/ml

4.2 Calibration

The calibration curve results from the analysis of the container. Multiple polynomial functions were used to determine the best fit. By using the known measurements of the container, it becomes possible to correlate the intensity of calcein emission with the thickness of the calcein solution. The first step is determining the best-fitting trendline to develop an algorithm that can provide the Thickness corresponding to a given intensity.

4.2.1 Third-order polynomial

Each horizontal line of the container is analysed to tie the thickness to intensity, which results in around 760 trendlines. These trendlines are averaged and used to calculate an average third-degree polynomial. As Figure 14 shows the multicolour band is all the raw data used to calculate the individual trendlines. However, looking at the raw data, artefacts caused inaccuracies to compensate for the first and last 50 pixels have been removed. A second-order extrapolation was performed from 0 to the first intensity detected to estimate the initial correlation.
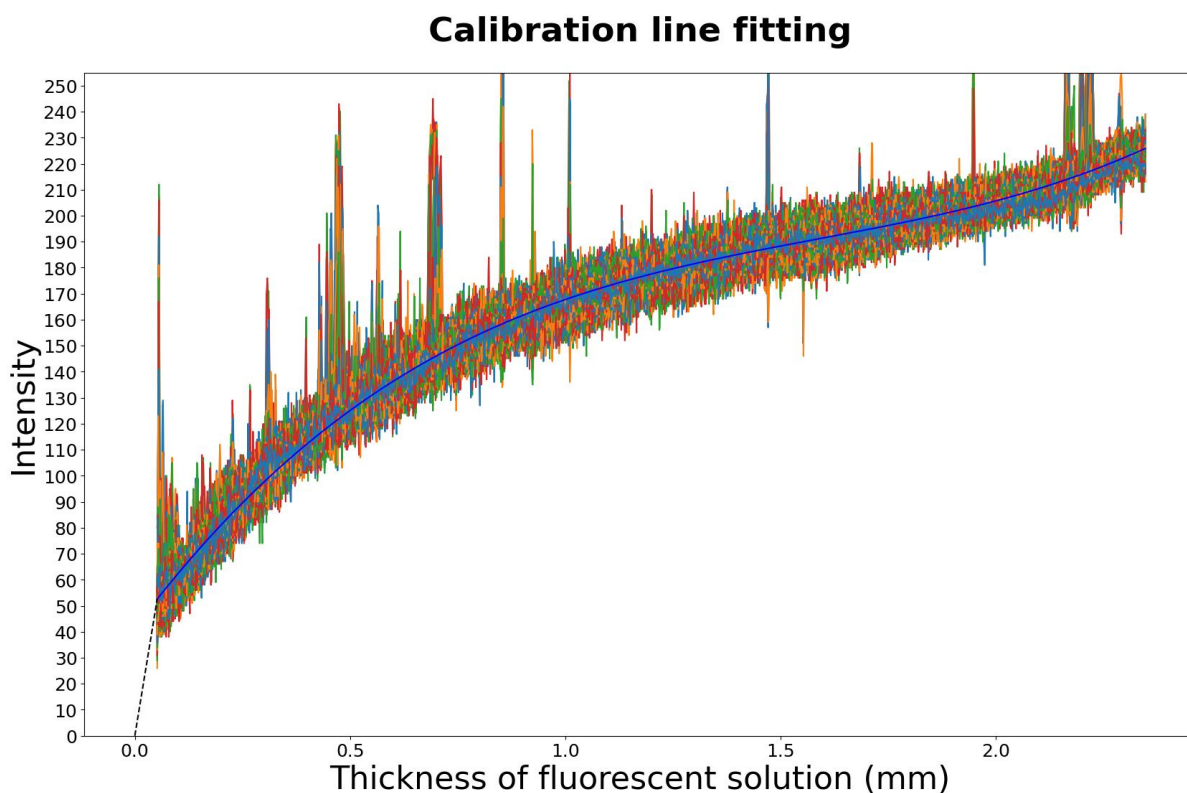
Figure 14: Displaying the raw intensity data collected from the calibration curve. The blue line is the average third-degree trendline, and the black dotted line displays the extrapolated second-degree fit.

The calibration was performed in a total of 14 times for 0.2 mg/ml calcein. Here a mixture of simply removing and replacing the container, and a complete washout, cleaning, and refilling the container were conducted. What was interesting was the division that can be seen in Figure 15. It shows there are two groupings, for which no explanation was found during this study. The four lower detected lines are from two different experiment days and both approaches. For volume analysis, this study selected the middle trendline provided by DSC_0725 (Figure 11B) to average the results of volume analysis.
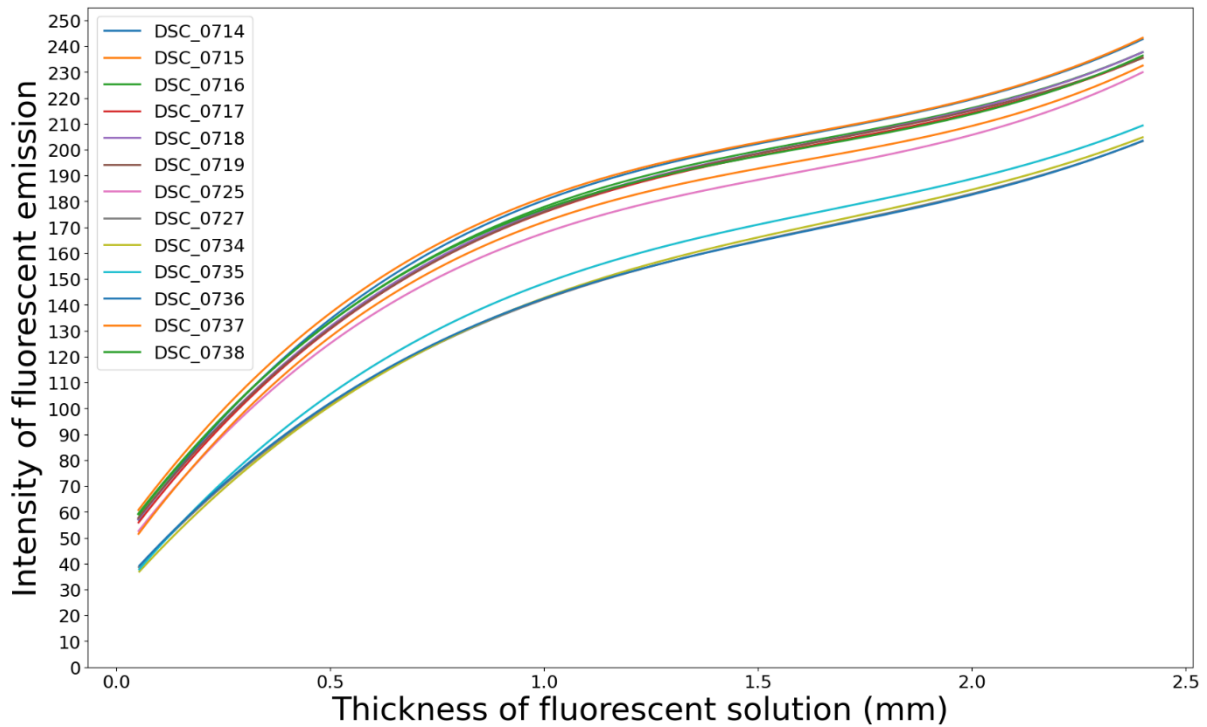
Figure 15: Displaying the average third-degree polynomial for several calibrations for 0.2 mg/ml calcein

Using the information gained from DSC_0725 the following second-degree polynomial was derived from the extrapolation:

$$Intensity = (-2.0 * 10^{-11} \, mm^{-2}) * Thickness^2 + 1011.60 \, mm^{-1} * Thickness + (1.06 * 10^{-15})$$

The reversal of this equation is used to calculate thickness at observed intensities up to 52 and will be referred to as low-intensity. This constitutes a thickness of 0.05 mm.

For intensities greater than 52, the third-degree polynomial is used to calculate thickness, which uses the following equation:

$$Intensity = 25.23 mm^{-3} * Thickness^3 - 119.913 \, mm^{-2} * Thickness^2 + (221.06 \, mm^{-1})$$
$$* Thickness + 41.41$$

The values acquired from this equation will be referred to as high-intensity.

Combining the two polynomials the thickness can be derived from every value in the intensity range. That can be used to calculate the volume using the formula established in section 3.3.2, as the area of a single pixel is fixed at 0.001187 mm^2.

4.2.2 Distance to camera lens

To establish the effect of distance in the 2D acquired image, an experiment was conducted where the container was shifted by 0.1 mm per picture from the default location. This distance shift led to a maximum difference of 1 cm, like the depth found in the Koken Model. As shown in Figure 16, a minimal shift is observed, comparable to the differences between calibration curves for a standard calibration. Therefore, it was concluded that the expected distance variance in the model would not impact the analysis significantly.
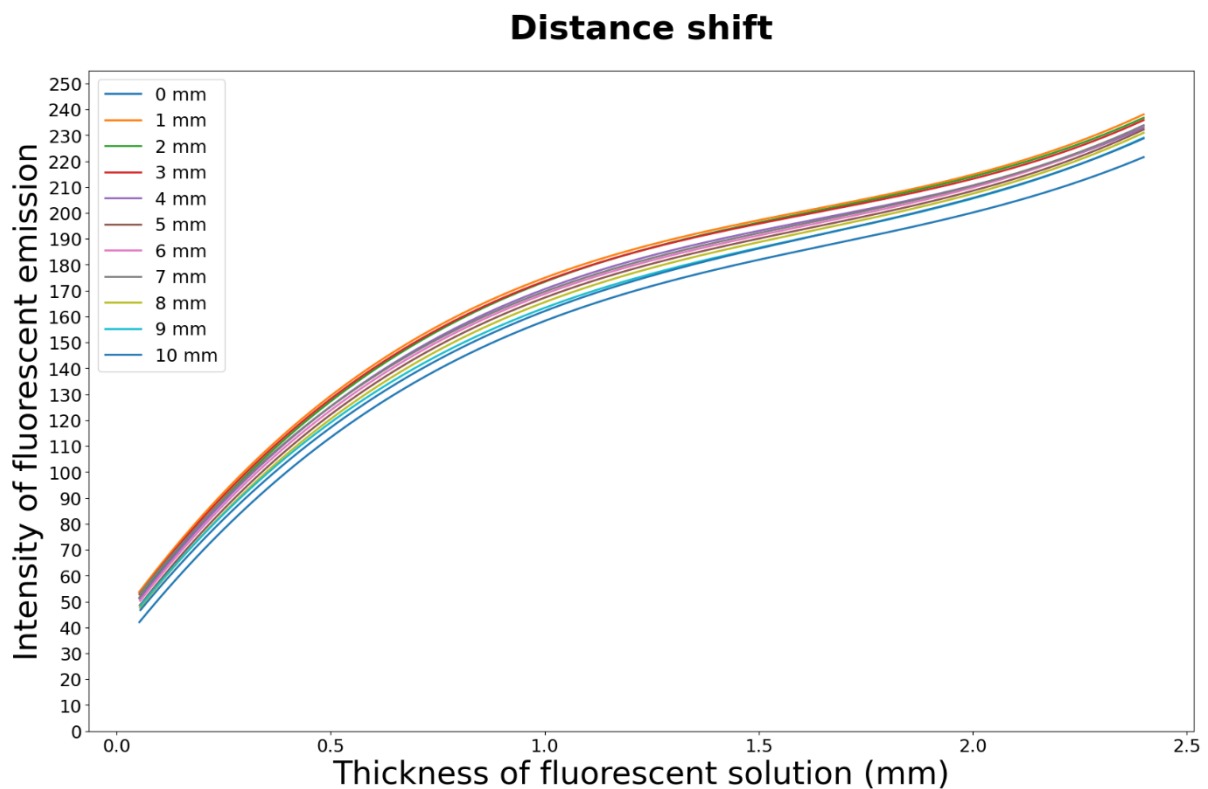
Distance shift

Figure 16: Showing the effect of shifting the distance from the container to the fixed position of the camera and light source.

4.2.3 layered effect

The thickness of the container wall impacts the calibration. To test this hypothesis, an additional wall was attached to the container, resulting in the comparison shown in Figure 17. Most of the differences are observed in the thicker calcein layers, where a decrease in intensity is seen with a thicker layer of Plexiglas. While Plexiglas is not UV-reactive, it lengthens the path of the green light to the camera. This can cause the pixels to be detected with lower intensity, resulting in a lower intensity at the same thickness layer of calcein.

Thickening of the container wall
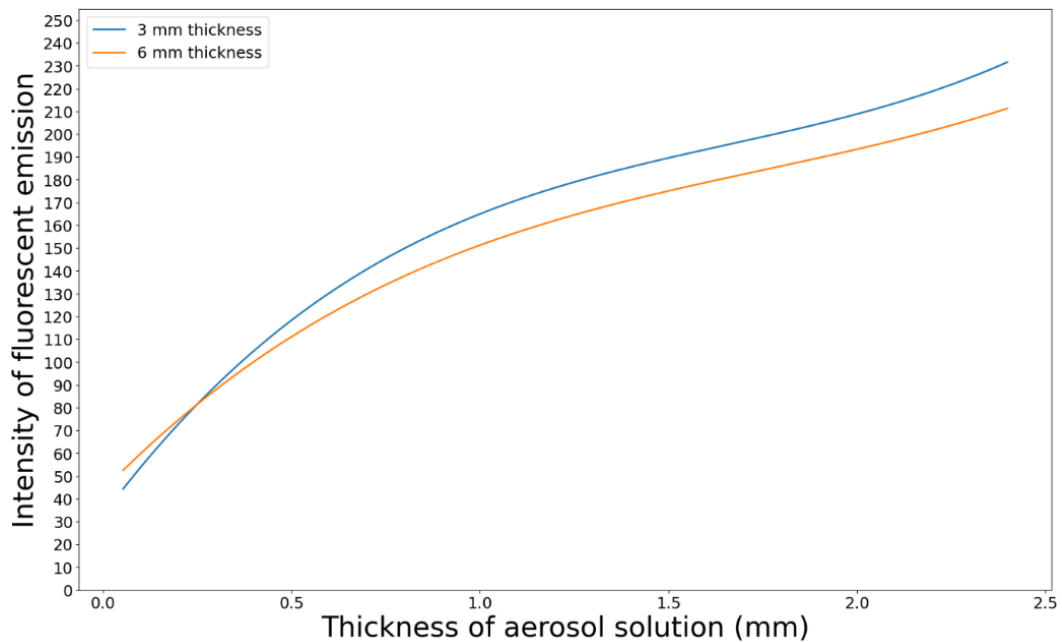
Figure 17: Showing the effect of different thicknesses in the plexiglass wall of the calibration container

4.2.4 Extra Thickness of calcein

By placing a microcuvette behind the calibration container an area was created that had maximum intensity as the thickness of the calcein in the microcuvette was 4.5mm. This was performed for both left middle and right placement to examine the effect of the added thickness behind the calibration container. Figure 18 shows how the microcuvette can be seen through the calibration container and strengthening the intensity at that location.
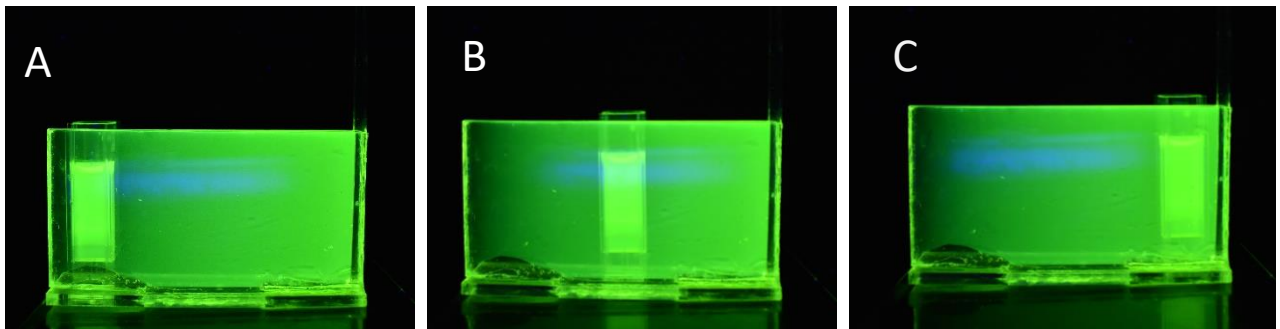
Figure 18: the visual information of how the microcuvette affects the calibration container and shows the effect of multiple layers of calcein deposition. A displays the placement on the left, B has the microcuvette in the middle, and C the microcuvette is situated on the right side of the container.

When looking at Figure 18 A the following raw data in Figure 19 is found when analysing the height where the microcuvette has an effect. It shows that the intensity goes to the maximum where the energy is combined and has a slight effect on the surrounding emission. When examining 18 B, Figure 20 displays the same effect of maximizing the emission of intensity in the green spectrum, however, the elevation is less gradient when compared to 18 A. 18 C demonstrates in Figure 21 a similar effect to 18 B.
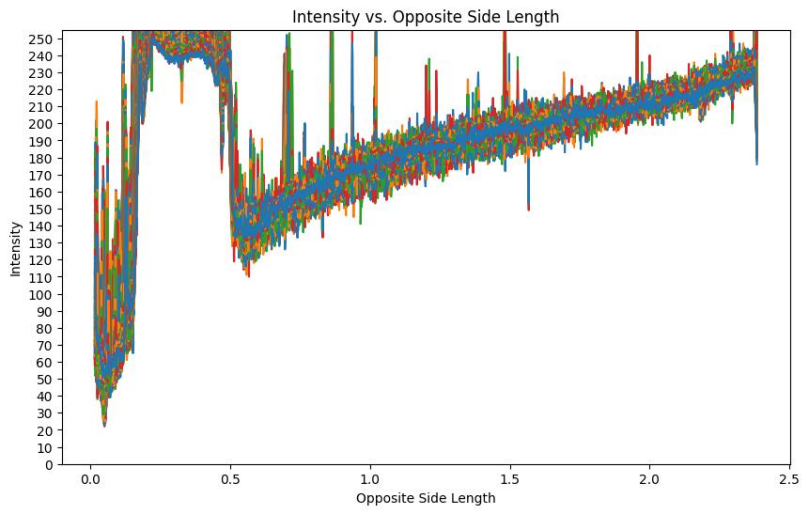
Figure 19: The raw data of the intensity compared to the thickness of the fluorescent dye of Figure 18 A
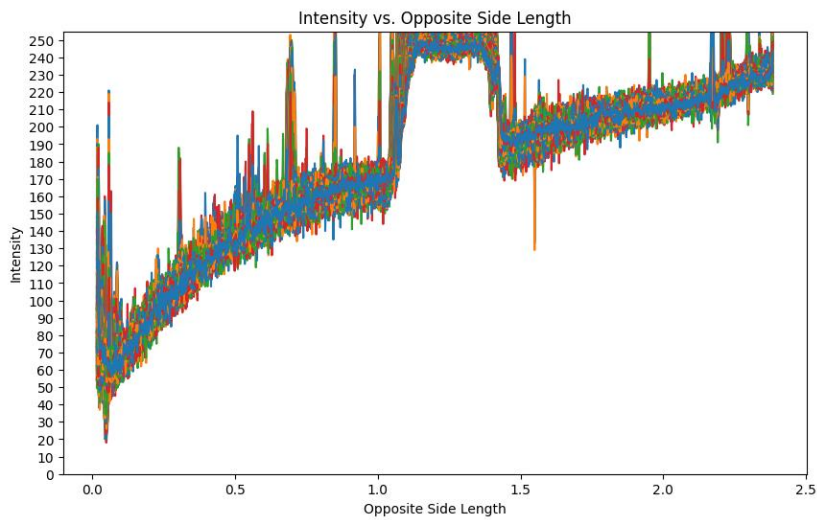
Figure 20: The raw data of the intensity compared to the thickness of the fluorescent dye of Figure 18 B
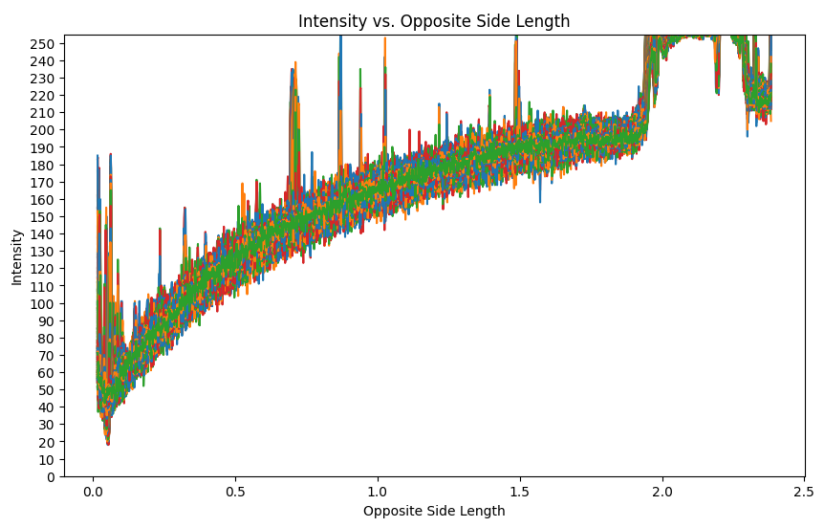
Figure 21: The raw data of the intensity compared to the thickness of the fluorescent dye of Figure 18 C

4.3 Volume quantification

The next step in developing a quantification method is to analyse the accuracy of the established calibration lines. Initially, this was performed by depositing controlled quantities on a flat surface to quantify the detected volume. The algorithm analyses the total area covered by the deposition. A division is made between the thickness that falls under the second-order polynomial and the thickness calculated by the third-order polynomial. The area and intensity of a single pixel are used to calculate the volume of the detected substance. As established in this study, intensity is directly related to the thickness of the calcein.

4.3.1 Flat Surface Analysis

Ten experiments were conducted where different amounts of solution were deposited using a 4 μm pore size soft mist nozzle attached to a syringe creating an atomizer. This created 10 different deposition patterns that could be used to analyse the accuracy of volume detection by the algorithm. Experiment 4 is shown in Figure 22, where a deposition pattern was created diversely. A total volume of 80.7 μl was applied to the flat outer wall of the Koken model.
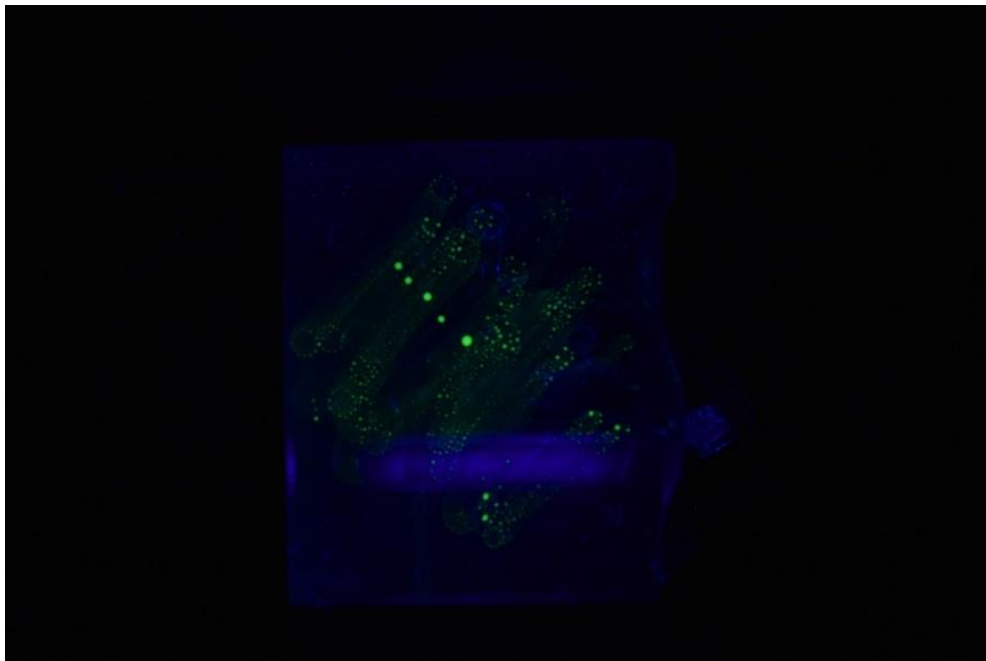
Figure 22: Showing a deposition pattern created by spraying the flat surface of The Koken nasal cast with a weighted quantity of calcein

Figure 23 displays the different thickness maps for the second-order polynomial and third-order polynomial derived from Figure 22, illustrating the algorithm's capabilities to detect the solution. By separating these two, a greater understanding of how the volume is distributed can be achieved.
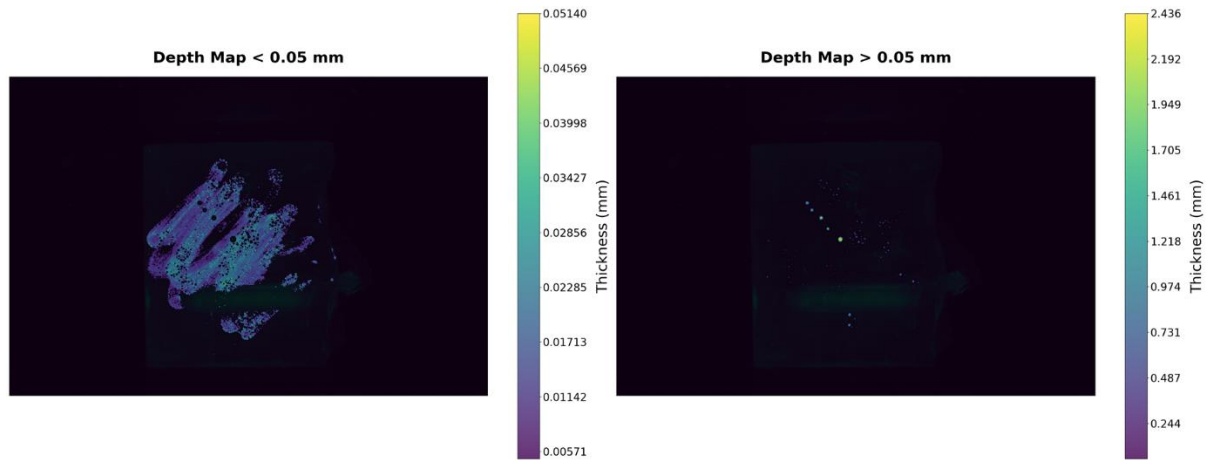
Figure 23: Showing the two different depth maps for Experiment 4, where on the left low-intensity and on the right high-intensity.

When examining the combined thickness map of the dispersal pattern, much of the resolution of the smaller particles is lost due to scaling, as seen in Figure 24. The resulting volume detected by the algorithm was 80.6 µl, underestimating the actual volume by 0.06%. The solution covered approximately 13.8% of the photograph, consisting of 3842.86 mm² surface area covered in low-intensity and 93.52 mm² in high-intensity. In addendum B.1, an additional experiment is shown for visualisation.
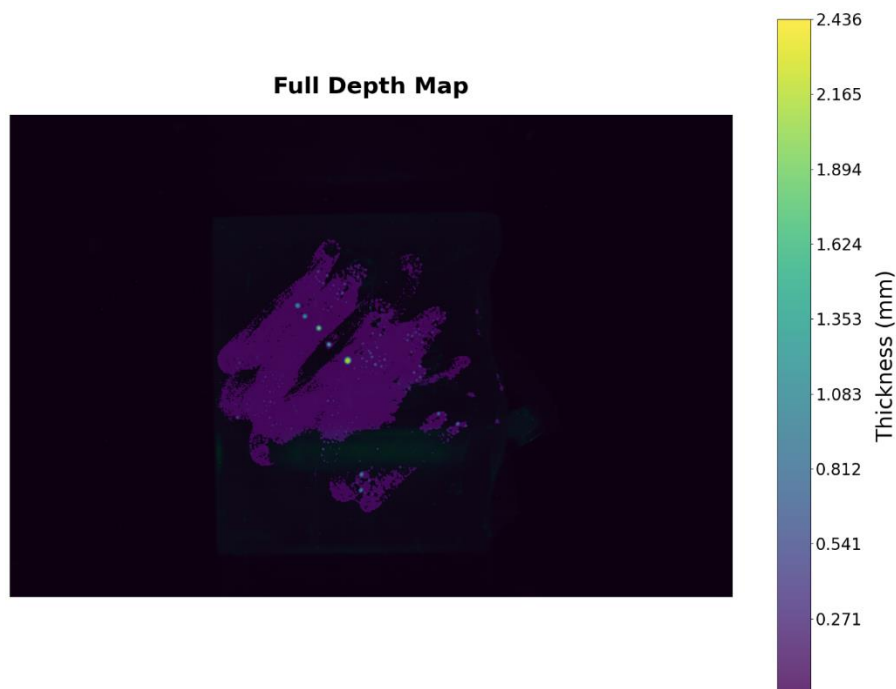
Figure 24: The combined depth map, showing all detected thicknesses of calcein deposition

Table 4 shows the 10 experiments that were conducted on the flat surface of the Koken Model. Deposited volume was the volume calculated by weighing the syringe before and after application. Here it can be observed that a wide range of different patterns was deposited from 39.5 µl to 116.6 µl. The calculated volume showed an overall accuracy deviation of around 17.2%, with the best estimation being -0.1% underestimation and an outlier of 44.0% overestimation as the highest observed deviation. Additionally, what can be observed is that most of the deposition made with soft mist nasal atomizer falls in the low-intensity thickness.

Table 4: The resulting analysis from the 10 experiments showing the values for volume and area covered.

Experiment	Deposited volume	Calculated volume	Recovery deviation	Area covered low-intensity	Area covered by high-intensity
	µl	µl	%	mm²	mm²
1	111.1	90.7	-18.4	3327	188
2	39.5	30.3	-23.3	2270	15
3	97.7	106.2	8.6	3155	213
4	80.7	80.6	-0.1	3843	94
5	86.8	69.7	-19.7	3837	58
6	116.6	128.3	10.0	4380	180
7	98.3	87.1	-11.4	4402	50
8	98.1	111.1	13.3	4433	64
9	55.7	80.2	44.0	2926	52
10	45.1	55.4	23.0	2643	42

4.3.2 Koken Model Analysis

The next phase of testing the algorithm was to deposit a predetermined quantity, similar to the flat surface experiment, in the 3D structure of the Koken model nasal cast. This resulted in patterns as seen in Figure 25. In this experiment, 89.6 µl was deposited over the internal 3D structure.
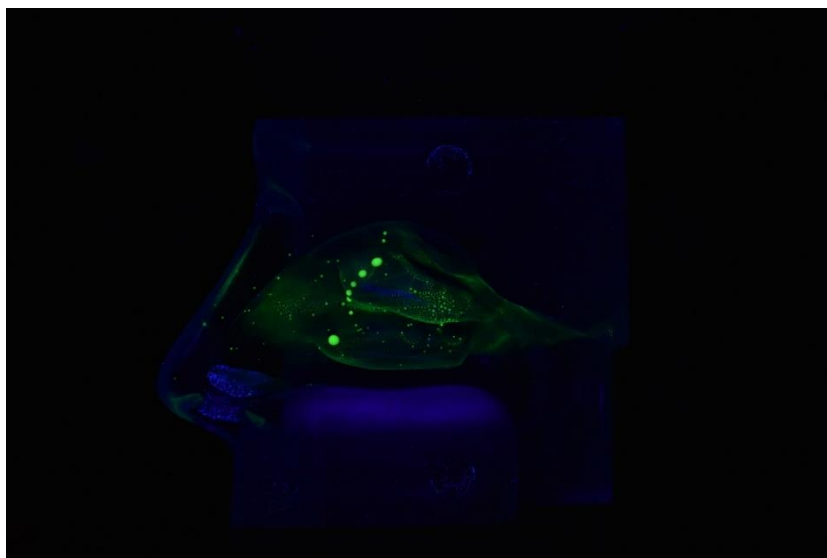
Figure 25: Showing the manually created dispersal pattern to examine the effect in a 3-dimensional environment

The original deposition image (Figure 25) and the thickness map (Figure 26) of experiment 15 show illumination in areas where the calcein was not deposited. The cause of this effect is related to the reflectance of the fluorescent emission on the 3D structure. This caused an overestimation of 12.6 %, resulting in a detected volume of 100.9 µl. For in-depth visualization, the separate depth maps for low and high-intensity can be observed in addendum B.2.1.
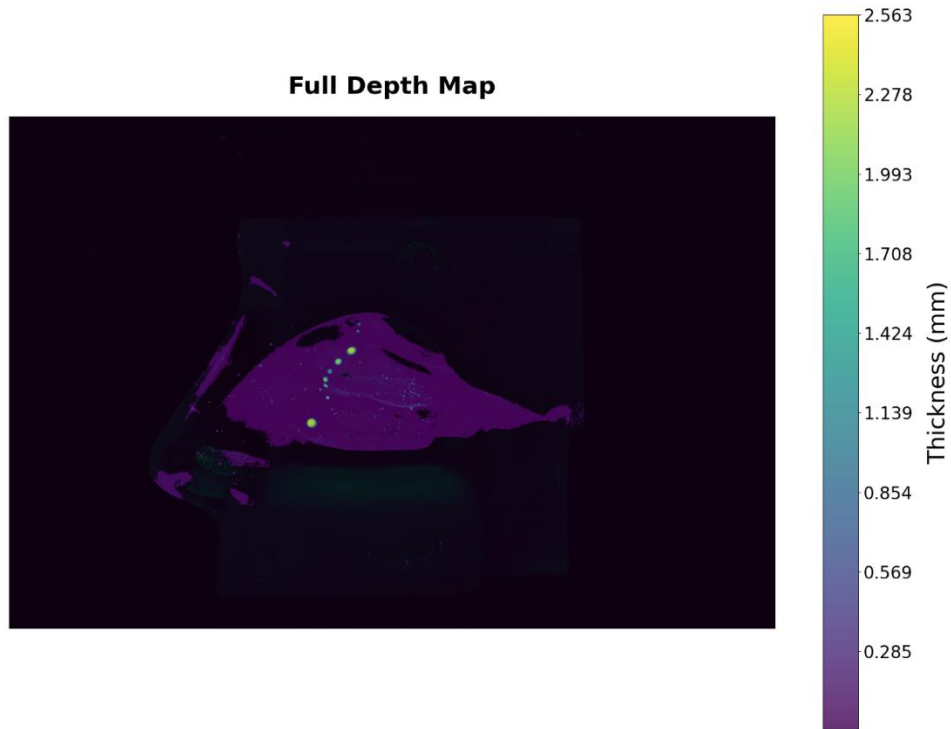
Figure 26: The resulting depth map using the image analysis software

Table 5 shows the resulting volumes calculated by the algorithm. The median of the overestimation is 27.5 % with outliers of 113.7 % and 62.9%. the hypothesis from this study is that the overestimation is caused by reflectance on the surface of the model.

Table 5: The data resulting from the volume analysis

Experiment	Deposited volume	Calculated volume	Recovery deviation
	µl	µl	%
11	145.1	309.9	113.7
12	151.0	186.4	23.4
13	61.1	97.9	60.2
14	130.4	166.9	28
15	89.6	100.9	12.6
16	127.00	161.2	27
17	171.1	205	19.8
18	107	125.4	17.2
19	104.7	170.6	62.9
20	155.2	218.7	40.8

The algorithm can further analyse how the volume is distributed over the surface area. Currently, this is performed using the two different equations as division. Table 6 shows the differences in volume distribution of the low-intensity and high-intensity equations. It demonstrates the capabilities of the algorithm in aiding the understanding of how volume is distributed with aerosol deposition. Overall, the manual application, shows that most of the volume accumulates in the range of the high-intensity algorithm, while the low-intensity covers most of the surface.

Table 6: Distribution of volume and surface area coated by calcein.

Experiment	Volume low-intensity	Volume high-intensity	Area covered low-intensity	Area covered high-intensity
	μl	μl	mm²	mm²
11	58.4	251.6	4015	564
12	62.5	123.9	4063	413
13	25.1	72.8	2357	62
14	48.2	118.7	3239	286
15	50.8	50.1	3452	130
16	49.8	111.4	3201	377
17	56.3	148.7	3620	456
18	44.7	80.7	3167	215
19	55.1	115.5	3556	334
20	48.1	170.5	3446	299

4.3.3 3D mask

To reduce the effect of reflectance a simplistic cropped image was loaded into the algorithm. The cut-out was limited to the sprayed area. Figure 27 showed an overestimation of 12.6% which was reduced to 1% for Experiment 15. This demonstrated the impact reflectance has on the algorithm.
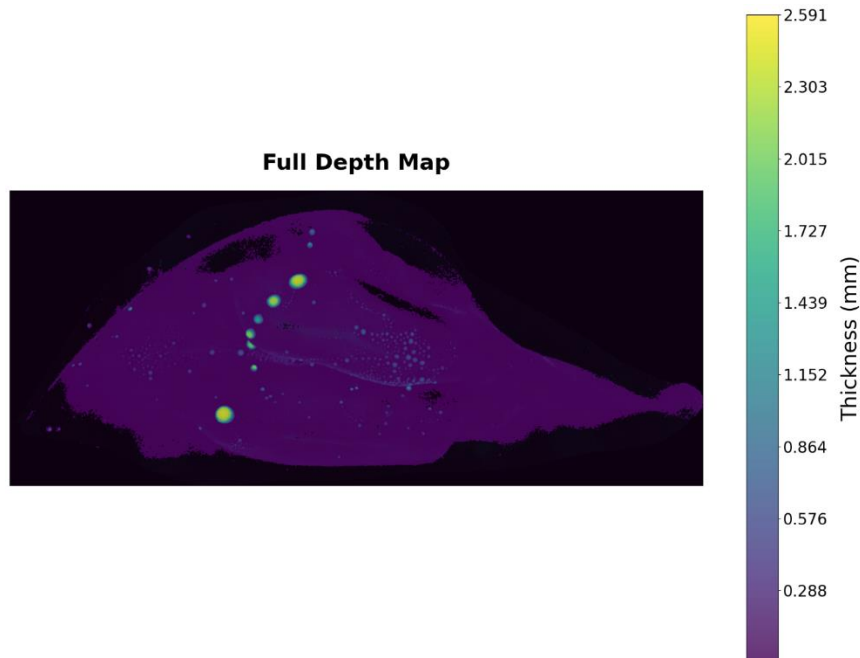
Figure 27: The depth map from a manually acquired mask from Experiment 15 to reduce the effect of reflectance

This manual approach has been performed for every analysis done in 4.3.2. This is displayed in Figure 28, showing an overall decrease in overestimation for every image by an average of 12%. The raw image and the low and high-intensity depth maps can be seen in addendum B.3.
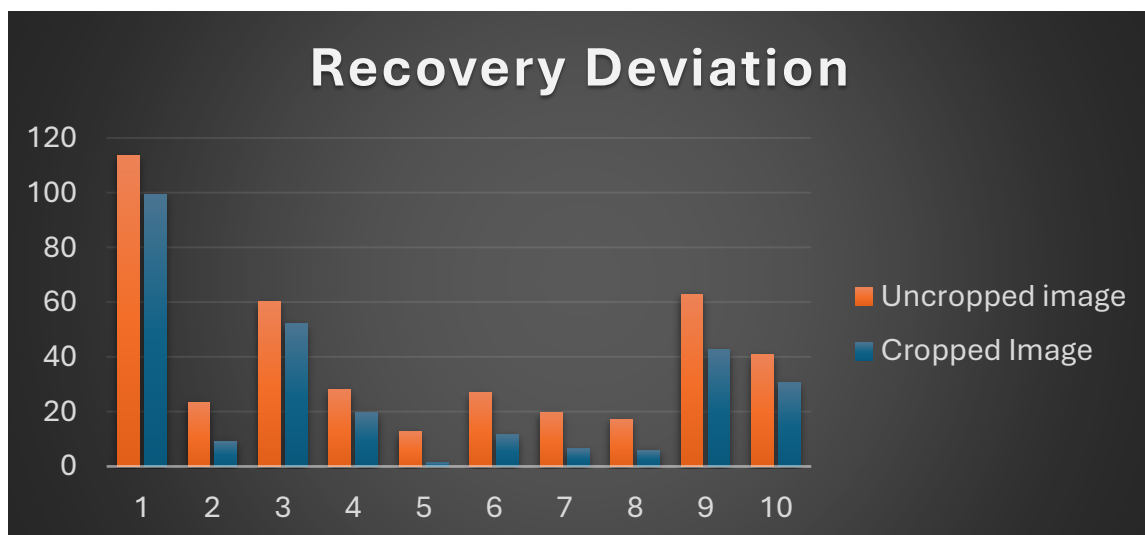
Figure 28: The percentage of overestimation in total volume. Where orange shows the value for uncropped images and blue displays the overestimation of cropped images.

4.4 Quantification of aerosol deposition

To test the algorithm with in vitro data, regular nasal spray deposition was created. Using the Standard Swirl nasal spray and the Soft Mist atomizer two patterns were created with 0 l/min airflow, and one image was acquired using 15 L/min airflow.

4.4.1 Standard Swirl Nasal Spray

From visual inspection of the nasal deposition created by the standard swirl nozzle, it was seen that the solution slid through the model due to the exit velocity of the nasal spray and accumulated in large droplets. These larger droplets also create more reflectance, which leads to an overestimation of the volume of deposition. In Figure 29, the resulting deposition pattern can be seen with 15 L/min airflow through the model. The deposited quantity in the model was 79.9 µl. However, the algorithm detected 108.4 µl, which is an overestimation of 35.6 %. This study hypothesises that the overestimation is caused by reflectance which is more prevalent with the standard swirl nasal spray. Most of the detected deposition is seen in the high-intensity range, namely 93.7 µl compared to 14.6 µl in the low-intensity range, despite the high-intensity range covering a smaller surface area of 80 mm² compared to 1766 mm². Further visualizations are available in addendum C.1.2.
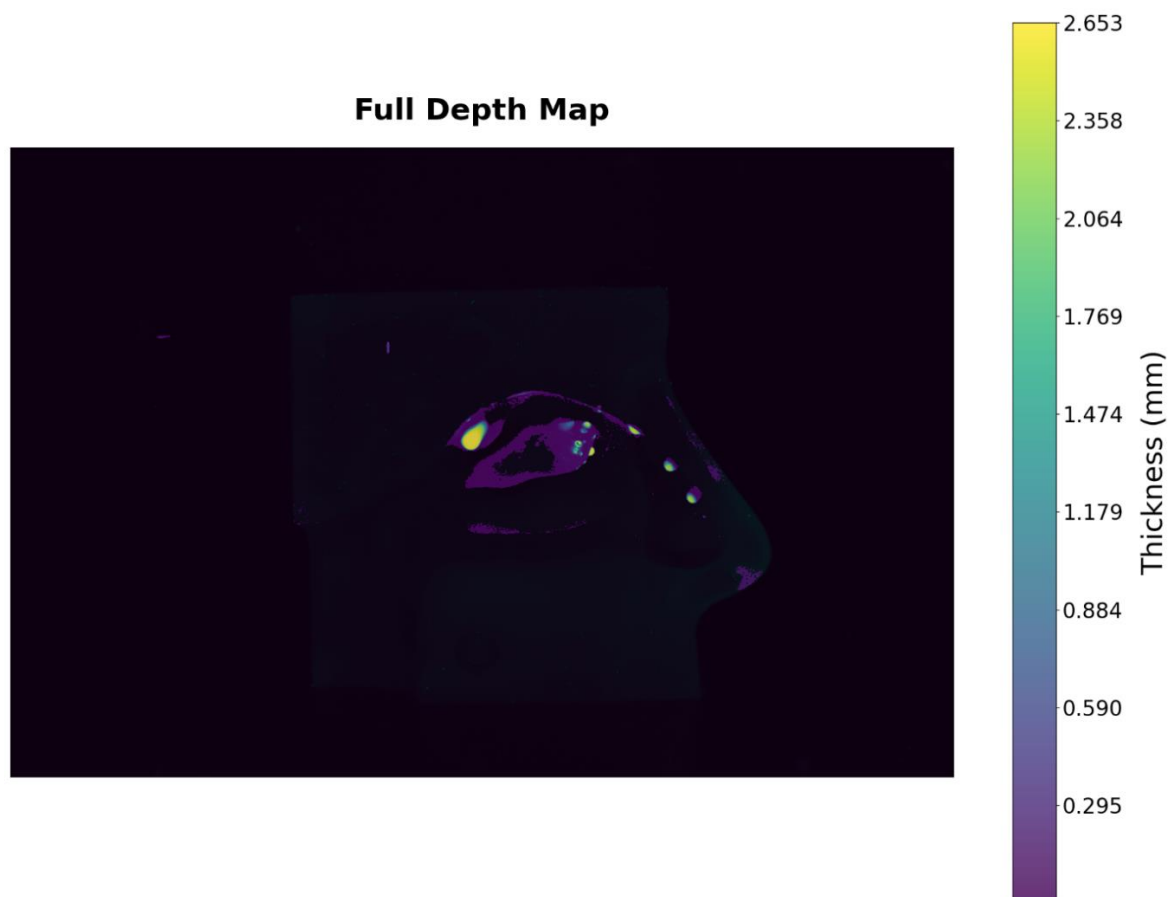
Figure 29: The resulting depth map was acquired from an aerosol deposition created with a swirl nozzle nasal spray with 15L/min airflow.

4.4.2 Soft Mist Nozzle Atomizer

The Soft Mist Nozzle displayed a more even coating behaviour, applying a more uniform coating in the nasal cavity. As can be seen in Figure 30, 2082 mm² was coated with low-intensity thickness, resulting in a volume of 22 µl. The high-intensity thickness covered an area of approximately 148 mm², resulting in a volume of 60.2 µl. Additional visualization of the thickness can be found in addendum C.2.2. The algorithm detected a total volume of 82.5 µl. With the actual deposited volume in the model being 82.2 µl, the recovery deviation is 0.3%. It was observed that the most deviation was found with the swirl nozzle around the thicker droplets of aerosol deposition.
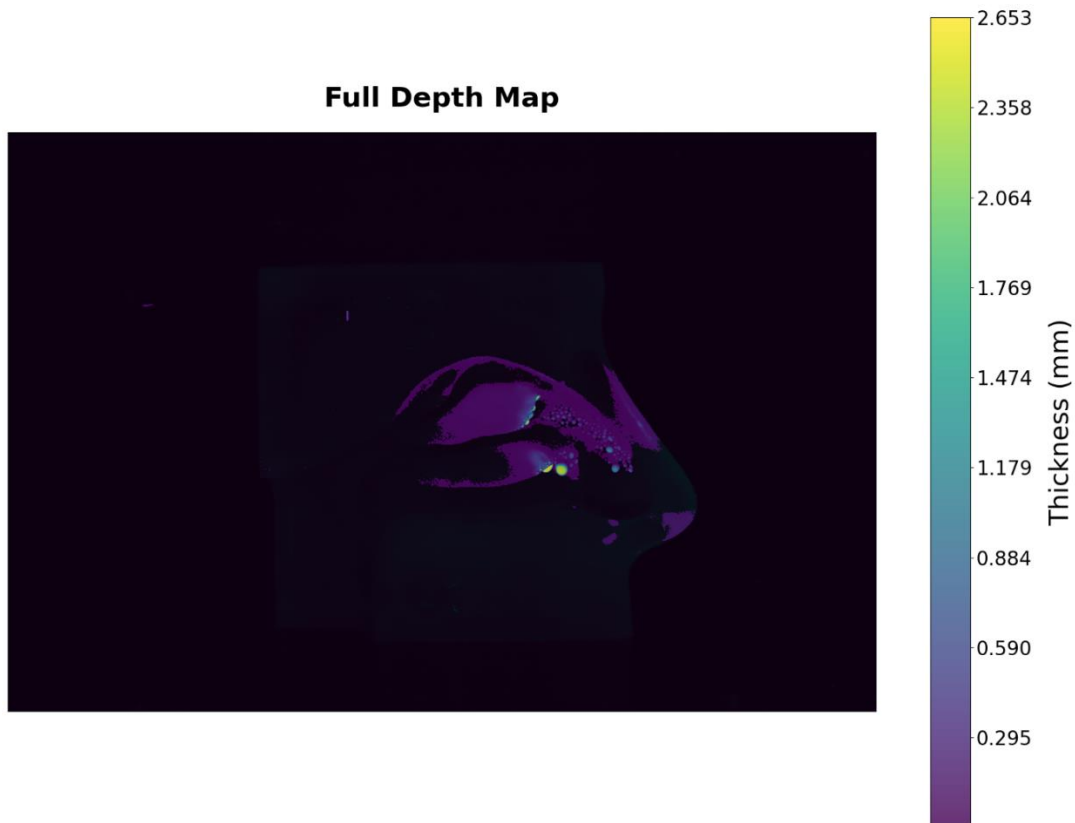
Figure 30: The resulting depth map was acquired from an aerosol deposition created with a Soft Mist atomizer with 15L/min airflow.

4.4.3 Comparison Standard Swirl nasal spray and Soft Mist nozzle Atomizer

From both the swirl nozzle and soft mist nozzle the first two measurements were conducted with 0L/min airflow, while the third measurement was performed with 15 L/min airflow. The raw images of the deposition patterns can be seen in C.1.1 and C.2.1 for the Standard swirl nozzle and soft mist atomizer respectively. What stands out is the overall lower recovery deviation from the soft mist atomizer compared to the Swirl nozzle. The expectance is that this is caused by the larger droplets that are formed by the standard swirl nozzle causing more reflectance. As shown in Table 7, the overestimation of the swirl nozzle was over 35%, while the soft mist atomizer had the highest overestimation of 9.6%. Additionally, more deposition was found on the divider with the swirl nozzle with no airflow. However, the soft mist showed a more susceptible to airflow as seen by the increased deposition lost on the divider of the Koken Nasal cast.

Table 7: The measured volumes during the application of the aerosol and the resulting total volume found in the model.

	Measurement	Volume Device	Volume Divider	Volume Model	Model volume found	Recovery deviation
		µl	µl	µl	µl	%
Swirl nasal spray	1	87.577	19.98	67.6	93.6	38.4
	2	87.665	34.85	52.8	79.1	49.7
	3	93.914	13.99	79.9	108.4	35.6
Soft mist atomizer	1	67.949	10.21	57.7	56	-3.1
	2	85.641	7.129	78.5	86.1	9.7
	3	120.85	38.64	82.2	82.5	0.3

By using the division in thickness from the two algorithms it can already be observed that 86.5% of the volume is deposited thicker than 0.05 mm across a surface area of 80 mm^2. For the soft mist nasal atomizer around 73.1% across 148 mm^2. The remaining volume was spread out over an area of 1766 compared to 2082 mm^2 respectively. Therefore, more volume is spread out over a bigger surface area with the soft mist atomizer. As can be seen, the low-intensity has the largest surface area with both methods of application of nasal aerosol. Table 8 shows the data acquired for all 6 measurements.

Table 8: Displaying how the different volumes from low-intensity and high-intensity are divided

	Experiment	Volume Low-intensity	Volume High-intensity	Volume Low-intensity	Volume High-intensity	Area low-intensity	Area high-intensity
		µl	µl	%	%	mm^2	mm^2
Swirl nasal spray	1	14.5	79.1	15.4	84.6	1711	83
	2	12.5	66.6	15.8	84.2	1577	71
	3	14.6	93.8	13.5	86.5	1766	80
Soft mist atomizer	1	18.6	37.4	33.2	66.9	1764	100
	2	19.3	66.8	22.4	77.5	1882	157
	3	22.2	60.3	26.9	73.1	2082	148

5. Discussion

The main goal of this study was to quantify aerosol deposition in a nasal cast, the results of this study allow for quantification of volume. The patterns of coverage seen visually are comparable to earlier results achieved by D'angelo, Kooij and Verhoeven et al.[1] Allowing users to adequately interpret the information provided by the quantification method it is important to understand all factors affecting quantification and aerosol deposition. This section will explore the factors that influence the calibration of the algorithm and the quantification of aerosol deposition in the nasal cavity.

5.1 Model, Analysis Method, and Material

Initially, the choices in the model, analysis method and material will be explored. While for this study the combination of these three elements fitted best with the objectives. It is important to understand the advantages and disadvantages of this approach.

5.1.1 The Koken nasal cast

Several studies have used the Koken nasal cast for aerosol deposition. It was found that there is a deviation from the anatomical structure found in living subjects. The cause of this is that the model is based on a deceased Asian female. It was found that leads to an increase in space in the nasal cavity. This allows for more airflow to move through the nasal cavity, which influences the dispersal pattern of the aerosol deposition. While it was found in a study that for the olfactory region airflow had minimal effect, other regions such as the middle turbinate displayed more influence under different airflows.[69] Therefore, it is important to understand how airflow differs in human subjects. The nasal cavity uses the turbinate's to optimize airflow for inhalation of oxygen.[3] It is this study's findings that a singular static model is unable to accurately describe real-life situations. While it allows for the development of an algorithm to quantify deposition with further analysis into the behaviour of nasal sprays it is important to test variances of models, to be able to understand how different airflow patterns influence the deposition.

Additionally, the Koken nasal cast is a transparent model. Due to this nature, it allows emitted light to be reflected off the surface. For the algorithm, there is no difference between reflectance and source emittance of the green fluorescence. Providing an explanation for the overestimation in the 3D structure analysis.

5.1.2 Photo Analysis

Aerosol deposition is a fourth-dimensional situation that occurs in a three-dimensional space over time. An image captures a two-dimensional snapshot of that occurrence after at least 10 seconds of deposition. More time will have passed as the deposition is performed outside of the dark box and placed in the box. This shows the fully set deposition in the model, however, this can also be influenced by the movement of the model. While this study hypothesises that the effect is minimal and an accurate representation of aerosol deposition is acquired, it can introduce inaccuracies in aerosol deposition.

The algorithm now in the two-dimensional spectrum was shown to add multiple layers of deposition. Therefore, the intensity increased at the location where for instance both the front and back of the

turbinate were covered by aerosol deposition. While providing information regarding overall deposition, information is lost in the manner the aerosol travels through the nasal cavity.

5.1.3 Calcein solution

When examining the excitation and emission spectrum of calcein, it shows that the excitation peak is at 501 nm and the emission peak is at 521 nm as can be seen in Figure 31 [70]. The UV light (ZLUVB, Velleman NV, Gavere, Belgium) emits at a frequency of 366 nm. Therefore, resulting in a suboptimal excitation of the solution. However, calibration and quantification are performed using the same UV light, which enters the same energy into the solution. This will allow for the suboptimal activation of the calcein to be similar in every experiment. It is important that when changing the UV light source with a different wavelength will cause a different intensity to return the fluorescence of calcein.

Additionally, it needs to be considered that the algorithm was developed based on the characteristics of a singular solution. Different solutions can change the fluorescent behaviour, which will lead to different calibration curves for the algorithm. As well as how the aerosol deposition will behave in the model and possible interaction with the material of the cast.
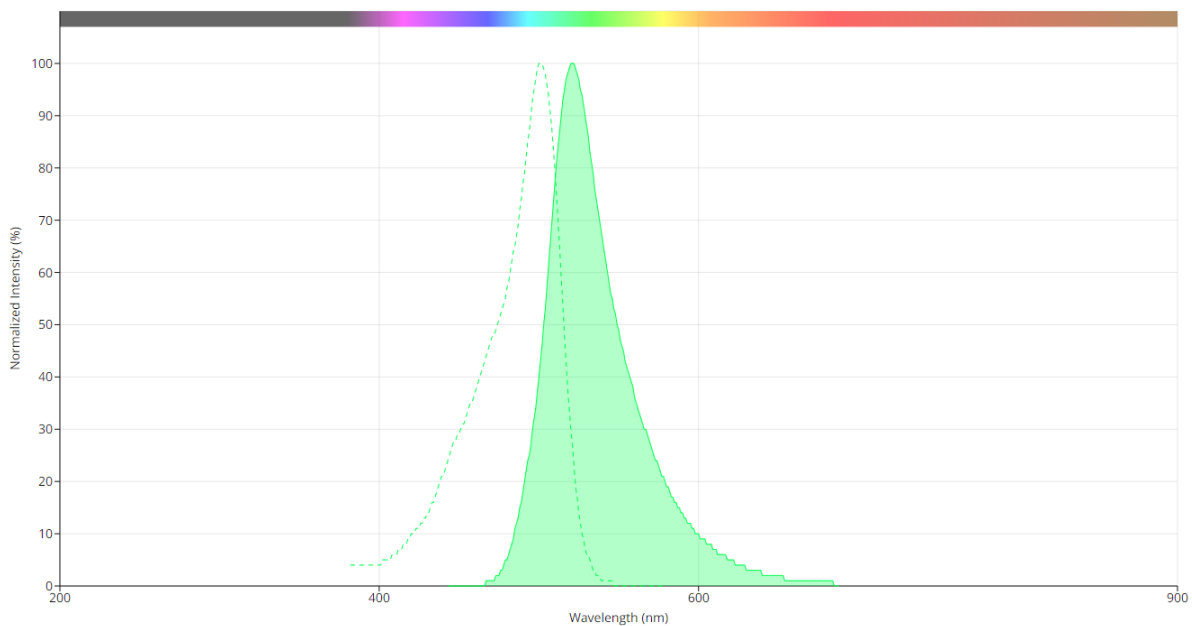
Figure 31: The emission and excitation spectrum of calcein[70].

5.2 Calibration

The core mechanic of the algorithm relies on the performance of calibration that ties the intensity to the thickness of the calcein. However, it was discovered that several factors influence the resulting calibration curve.

5.2.1 Fitting Line

Multiple orders were examined to establish a calibration line. The initial hypothesis posited that intensity was correlated to the thickness of deposition in a second order, due to the range of 0 to 255. However, upon examining the data, it was observed that the resulting trendline did not accurately fit the data. Mainly deviations were still observed in the lower and higher range of the

algorithm. To further improve accuracy, a third-order polynomial was established, resulting in the trendline shown in Figure 15. Higher-order polynomials were tested but did not provide further improvement in estimation and only increased algorithm complexity without additional accuracy benefits. A logarithmic approach was not performed by this study and could possibly better describe the intensity-thickness correlation.

5.2.2 Variance in calibration

There were 14 different calibration curves created, these showed variance in initial intensity and end intensity. While the shape of the curve appeared similar as can be seen in Figure 15. It was observed that there was a separation that caused two groups in calibration curves. This study did not find an explanation for the division. While there are factors that influence the calibration. The thickness of the plexiglass is such a variable that decreases the intensity of the calcein's emission pattern. However, all measurements were done with the same container and divided over multiple days.

On both ends of the division, calibration curves where the container was completely cleaned and placed in the dark box, as well as simply removing and replacing the container were performed. This, therefore, rules out any indication that over time the calcein solution causes changes in the calibration curve.

A theory is constructed that it can be a combination of factors that differ between pictures. As the camera is placed a new between every image due to resetting of the timer, this can cause a slight shift in position. The UV light is turned off between each image which might cause a slightly different input energy between acquisitions. Additionally, the container might be slightly shifted in position which can also cause alterations in intensity. Further research into these factors can help better the understanding of the emission pattern of calcein in combination with these elements to create a more robust calibration curve. This study due to time constraints chose to continue further examination of the quantification method with one of the average calibration curves observed in Figure 15.

When performing quantification, it is important to be aware that the deviation in calibration can cause different volumes to be found. If the volume deviates more than 20% from the inputted volume. One solution can be to recalibrate as an overall deviation might be caused due to the second and third-order polynomial.

5.2.3 angle

The container is placed manually in the dark box, while it is placed similarly every time a calibration analysis is performed, a shift in the angle of the container will create differences in the thickness that contribute to every intensity. This can cause inaccuracies in the resulting curve. Even though minor shifts in distance have been shown to impact the calibration curve changes only minimally in intensities at different thicknesses can cause a different calibration curve, which reduces the accuracy of the algorithm.

5.2.4 Camera position

As stated in 5.2.1 the camera is removed and placed in the dark box to activate the 10-second timer. This can cause a slight shift in pixels which can entail that the size of a pixel is different between pictures. This can cause variance in the thickness steps found using the calibration container. This is

partly compensated by manually finding the left and right boundary of the container and upper and lower limits.

Additionally, this shift plays a factor in the quantification of aerosol deposition. As the size of a pixel varies between images a difference in volume can occur. The easiest manner to solve this problem would be to reexamine the pixel size for each image and input the value manually. A more robust manner that can solve this is to incorporate landmarks in both the calibration container as well as the Koken nasal cast. D'Angelo, Kooij, Verhoeven et al have implemented a small marker to the right half of the Koken nasal cast as a marker.[1] However, this marker is a small pocket of calcein. Therefore, the analysis will see this as deposition when analysing the full image. The advice of this study would be to implement a marker that can be found in the red channel of the image. Currently, this colour channel is not used and can therefore be used for placement validation without interfering with the analysis.

5.2.5 UV-light strength and location

The placement of the UV light also has shown an influence on the intensity of the emission spectrum of calcein. Due to not optimally exciting the calcein variations between measurements can occur, when either the light is shifted or the strength of the light changes due to discharge of the battery. Additionally, it was observed that the UV light needed a minute to reach maximum illumination. These variances can cause a decrease in intensity emitted by the calcein and need to be accounted for.

5.3 Model Analysis

Overall, the algorithm proved to display a robust method for analysing volume detected through the algorithm. The algorithm was able to separate the background from the calcein solution and detect the deposition in different circumstances.

5.3.1 Flat Surface Analysis

The first phase was to test the algorithm on a flat surface. It was found that the variance of the recovery deviation was 17% absolute, where the algorithm underestimated and overestimated the actual measured aerosol quantity. This was found to be an acceptable margin when quantifying aerosol deposition. This showed that the calibration curve used to determine the volumes in these 10 deposition patterns was able to detect the quantity deposited and provide an analysis of the area that was covered and the manner the volume was distributed. This allows researchers to obtain a better understanding of the behaviour of Nasal sprays.

When examining the flat side of the Koken nasal cast it can be observed that the UV light reflectance is seen in the blue spectrum of the image. This reflectance overpowers the green emission of the calcein, which creates a zone where data is lost. Therefore, can cause a lower estimation due to an area not being measurable due to this artefact.

5.3.2 Koken Model Analysis

When examining the performance of the algorithm in a three-dimensional environment. It was discovered that the algorithm had an overall overestimation of an average of 27.5%. An explanation for the cause of this overestimation is the reflectance of the light on the geometrical environment of

the deposition. As light is reflected on non-coated surfaces this causes the algorithm to overestimate the volume. When limiting the analysis area to just the internal structure of the nasal cavity where the nasal spray was applied, a decrease in overestimation was found. Overall, it lowered the overestimation on average by 12%. While neither completely removing the effect of reflectance nor solving the overestimation completely it does provide a more accurate approach when analysing the nasal cast.

5.4 Quantification of aerosol deposition

The first notable difference is the pattern that is created by aerosol deposition. Where the Swirl Nozzle creates more focal points wherein the aerosol deposits, the Soft Mist nozzle a finer layer is created. Where the swirl nozzle had around 85% in the high-intensity and for the Soft Mist nozzle that was 75%. This study hypothesizes from this data that even further division in the different layers of thickness, more performance differences will be found in how the aerosol coats the nasal cavity.

Due to the Swirl nozzle creating larger droplets in the cavity, more reflectance is seen across the model. Which leads to a 40 percent overestimation compared to the five percent seen with the soft mist nozzle. Therefore, when examining thicker layers of aerosol deposition, it can be prudent to coat the model in a substance that negates light reflectance to minimize this effect further.

Another difference is the effect of airflow. Both nasal sprays were shown to be affected by airflow. The Swirl nozzle showed that more deposition was deposited on the model and not lost on the divider, while the soft mist nozzle showed the opposite effect. Additionally, it allowed the Soft Mist Atomizer to achieve a better penetration of the model surface. As stated in 5.1.1 the region most affected by airflow is the respiratory region as that structure is designed to optimize its function by controlling airflow. It is important to examine the nasal sprays in different circumstances. Especially when targeting specific regions such as the respiratory region. The olfactory region is less influenced by different airflows through the nasal cavity, but different behaviour in different regions of the cavity can lead to a different volume distribution.[69]

6. Future development

There are several factors that this study recommends for progressing the algorithm and further improving understanding of aerosol deposition using different types of nasal sprays.

6.1 Analysis improvements

Several steps in the algorithm rely on manual interaction. Currently, the user needs to select the edges of the container and the upper and lower limits of the calibration container in an image processing program such as ImageJ. Automating this process will allow for the reduction of human error in the placement of pixel location. This will allow for higher precision in the accuracy of the average trendline.

Whereas with the current container, there are artefacts present on the outer edges. Currently, the algorithm compensates by removing 50 pixels on both sides of the horizontal line used in the analysis. This causes the trendline measured from the container to not start at 0 mm thickness. This is solved by extrapolating the secondary polynomial between 0 and the initial value of the trendline to estimate the nature of the trendline. As this is an approximation, by improving the container a more reliable calibration curve can be achieved.

The volume quantification algorithm analyses the entire image for intensity to detect the thickness of the deposition and translate that to volume. There are, however, several parameters tied to markers in the image. For instance, the area of a pixel is tied to a reference marker, namely the outer edges of the model. In this study manually acquired from a singular image in the experiment. A slight shift in the model can constitute a change in the area that a pixel describes. When that changes the resulting volume in the algorithm, will also be different from the actual deposited volume. This can be improved by automating the detection of a landmark to determine pixel size and surface area.

6.2 Parameters Influencing Quantification

In this section parameters that affect both calibration and nasal aerosol deposition. Some of these parameters are discussed in Section 5, as preliminary investigation was needed to determine the effectiveness of the algorithm. However, further investigation is required to establish the full scope of external factors that impact measurements. This can then be used to determine boundaries for acceptable measurements.

6.2.1 Parameters

6.2.1.1 General parameters

Several parameters directly influence the performance of aerosol deposition. The parameters fall into three categories influencing calibration and aerosol deposition experiments. The first category is environmental and situational factors affecting calibration and aerosol deposition. Environmental temperature, solution temperature, solution preparation, UV light, Camera, and dark box. The effects of these parameters are not all in equal, however, none of these factors can be fully eliminated. Further experiments to establish the full scope of the impact will lead to a robust analysis of the aerosol deposition in the nasal cavity.

6.2.1.2 Calibration parameters

The second group of parameters mostly influence the calibration of the volume calculation. Currently, the container used to calibrate the polynomials is a prototype. Therefore, the container itself has some issues that can be solved and parameters that will influence the accuracy of the measurement. The used plexiglass has no interaction with UV-Light. However, it does cause a dimming effect that has been seen when examining it under thicker layers of plexiglass as described in 4.2.3. Additionally, there are artifacts on the edges of the container due to reflectance of the calcein and the angle of the corners influencing how light is redirected towards the camera. The placement of the container influences how the camera. For best result the container needs to be level and placed in a horizontal angle from the camera. This influences the thickness calculation of the polynomials which can cause a deviation from the actual values.

6.2.1.3 Nasal spray quantification parameters

The final set of parameters discussed here influences the application of aerosol into the nasal cast. The velocity of the nasal spray influences how the particles behave inside the nasal cast. This parameter is caused by the exerted pressure on the pump. Therefore, pressure is another parameter that influences the deposition patterns. The attributes of the solution impact how the droplets are formed and how they deposit in the nasal cavity. These consist of viscosity, density, size of droplets, and solubility of particles in aquatic-based formulation. The material of the cast also impacts how aerosol deposition is created. A human nasal cavity has the mucosa layer and cilia that influence how air and particles travel through the nose and bind with the nasal wall. The Koken model is a silicon surface that lacks either structure, while that can greatly influence the effectiveness of a nasal spray.

Finally, how the user applies the nasal spray additionally alters deposition. The angle at which the device is placed alters the path of the aerosol and how it will deposit in the nasal cavity. How the nasal spray is used, has an impact on how well the aerosol can spread through the nasal cavity. A fully pressed activator will use the full force of the nasal spray; however, only partial activation can cause less pressure to be exerted. This can constitute a lower velocity and lower volume being sprayed. The breathing technique and airflow through the cavity have an additional influence on how deposition is distributed through the cavity. While the study of Zhang, Verhoeven, and Ravensbergen et all, demonstrated that some regions are more affected than others, it is a factor that cannot be dismissed when trying to correlate in vivo analysis to in vitro hypotheses. [69]

There is a lot of correlation between the parameters of how aerosol deposition is created in the nasal cavity. Extensive research into how these correlations influence one another is valuable for advancing the development of the nasal cavity as a primary route for medication applications.

6.2.2 Proposed Parameter Evaluations

There are correlations between the different categories of the parameters mentioned in 6.2.1, therefore, these parameters need to be tested in controlled environments to establish the impact on calibration and quantification methods. This study wants to propose X experiments to evaluate the parameters that affect both the calibration and quantification of aerosol deposition.

6.2.2.1 Calibration evaluation

The largest influence on overall calculations is the calibration. An experiment with a new prototype of the container can evaluate the method. Additionally, this study hypothesizes that wall thickness

causes an overestimation of thickness in the Koken model. As shown in section 4.2.3, the preliminary investigation indicated that the resulting trendline decreased when a thicker wall was applied. Therefore, creating several containers with the same thickness gradient but varying wall thicknesses will provide insight into how the layered effect alters the calibration. By using containers with different wall thicknesses and maintaining similar external factors between measurements, it will be possible to evaluate the layered effect accurately.

Another layered effect not fully evaluated in this study is how the emission spectrum interacts with separate layers of calcein deposition. With multiple containers, preferably two with the same wall thickness, it can be determined if the emission intensity is additive or if there is a different correlation. Since the nasal cavity is a complex geometric structure, it is important to fully evaluate the calibration accuracy.

When examining these two parameters, it is crucial to keep the container perpendicular to the camera to ensure the analysis is performed without angular deviation. Differences in angle can cause a shift in actual thickness, leading to a discrepancy between the allocated intensity to the calculated thickness and the actual thickness.

By filling these containers with the 0.2 mg/ml calcein formulation, the data can be compared to earlier calibration experiments. This comparison will provide a better understanding of the parameters affecting calibration, allowing for the establishment of acceptable calibration windows.

6.2.2.2 In vitro parameters analysis

External parameters and aerosol parameters are factors that impact the overall performance of deposition creation. To calibrate effectively, more factors are controlled to create a constant environment. This study advises exploring parameters that influence deposition patterns. By shifting application parameters while keeping others constant, researchers can establish correlations.

External airflow can simulate how particles are guided through the nasal cavity. However, this will vary with different application angles and particle velocities. Therefore, shifting the airflow while keeping the application angle and velocity constant will demonstrate how airflow affects these two parameters. Based on the findings of Zhang, Verhoeven, and Ravensbergen et al., it is advised to use airflow rates of 0 L/min, 7.5 L/min, 15 L/min, and 25 L/min. These airflows are consistent with patients' possible inhalation techniques.[69]

Repeating the same steps for different angles while keeping airflow and velocity constant is essential. On average, patients have been found to insert the nasal pump at an angle between 45 and 60 degrees. [69] Therefore, it is recommended to vary the angle between 40 and 65 degrees, with a step size of 5 degrees, to investigate how the angle affects the deposition of aerosol.

The swirl nasal spray and soft mist spray have different particle velocities. The swirl nozzle particle speed ranges from 15 to 20 m/s, while the soft mist spray has an overall particle velocity of around 0.8 m/s. These differences arise from the distinct methods of aerosol dispersal, as explained in section 2.3. This study hypothesises that with higher velocity, airflow will have less impact on aerosol deposition. The study advises initially performing parameter analysis with the soft mist nasal atomizer and then repeating these experiments with a traditional swirl nozzle. It will be necessary to create a range of multiple speeds around the working velocity of the nasal spray to investigate the

correlation with other affecting parameters. For the soft mist nozzle, the advised steps are 0.4 m/s, 0.8 m/s, and 1.2 m/s.

This will result in an experiment initially using the soft mist nozzle, where four different airflows, five different angles, and three different velocities can be compared to establish their underlying correlations. This provides a basis for understanding how these parameters influence aerosol deposition in the nasal cavity.

6.3 Implementing Region Mask

Automating the pixel size detection introduces another improvement. It will allow for the introduction of region masks. This will make it possible to apply masks that highlight different regions in the Koken nasal cast. The first benefit achieved by applying masks will be that it reduces the impact of reflectance from outside of the deposition area. The effect this will have been already seen when manually applying a mask as described in 4.3.3. This reduced the overestimation by 12%. The expectance is that some of the seen deposition by the algorithm is still caused by reflectance, as that will be within the targeted area of the mask it will limit the overall impact.

Secondly, with the application of masks better understanding of the regional deposition of the nasal sprays can be achieved. By limiting the algorithm to specific areas such as olfactory and respiratory regions, a better understanding of how the volume distributes through the nasal cavity can be acquired.

6.4 Extensive comparison

This study made a short comparison between the swirl nozzle and the soft mist spray nozzle. While visually in the thickness map differences can be observed in how the two aerosol dispersal methods create their patterns. By performing a more in-depth analysis of how the calcein is distributed throughout the nasal cavity.

The first recommendation is to further divide the layers in thickness in how the calcein is spread through the cavity. Visually it can be seen that the swirl nozzle creates larger droplets where the solution collects in the cavity, whereas the soft mist spray creates a more spread-out pattern where the solution is deposited. By introducing more divisions in thickness levels, a more in-depth analysis is possible of how the nasal aerosol deposition is distributed throughout the nasal cavity.

6.5 Different types of nozzles

In development at Medspray are soft mist nozzles of different pore sizes. The difference in pore size influences the particle size created that forms the resulting mist. This study hypothesises that different particle sizes will change the way airflow and other external factors influence the distribution pattern of the aerosol. It is important to understand this influence on determining the differences between pore sizes. With this understanding, the right pore size can be chosen for specific desired distribution patterns.

6.6 Nasal Spray Performance Analysis

With that understanding, it becomes possible to create hypotheses describing the expected effect of different nasal sprays and the effect of medication administration. This data can then be translated to in vivo experiments to create clinically relevant information.

As stated in this paper, there is great anatomical variation between people that changes based on environmental circumstances. Therefore, this approach cannot substitute clinical studies on the effects of medication on human subjects. It is important to further analyse the beneficial effects of the soft mist nozzle to be tested in vivo trials.

In the current state, this approach is not viable for in vivo trials. This relies on imagery acquired from a specific distance that the algorithm is calibrated to. Further study into adaptation will be required to determine whether the algorithm can be adapted to a method that can be used in vivo, or if other analysis methods such as scintigraphy are better suited for in vivo trials.

7. Conclusion

The combination of the Koken Nasal cast, photo analysis, and fluorescent dye has proven to be a viable method for quantifying aerosol deposition. This method can detect deposition patterns and allow for volume quantification within a margin of error of 17%. Previous studies were only able to determine coverage, whereas this study was able to determine the volume of deposition. This advancement allows for further study into the behaviour of aerosol deposition.

When comparing the Swirl nozzle to the Soft Mist nozzle, it is observed that the Swirl nozzle creates large focal points where the aerosol accumulates in large droplets. In contrast, the Soft Mist nozzle creates a more evenly spread-out distribution of the aerosol. This distinction is evident in the division between low and high-intensity thickness maps. However, it is speculated that the high-intensity thickness map can be further divided into more categories, which would provide additional information on how these different types of nozzles create aerosol dispersal in the nasal cavity.

Therefore, this study concludes that photo analysis using a transparent model with fluorescent dye can adequately be used to quantify aerosol deposition.

8. AI usage

This study has made use of artificial intelligence in the form of ChatGPT for spelling and grammar checks. Additionally, AI has provided support for the development of Python code in the form of understanding errors. No further use of AI was made.

9. References

1.   D'Angelo D, Kooij S, Verhoeven F, Sonvico F, van Rijn C. Fluorescence-enabled evaluation of nasal tract deposition and coverage of pharmaceutical formulations in a silicone nasal cast using an innovative spray device. *J Adv Res*. 2023;44:227-232.

2.   Jones O. The Nasal Cavity - Structure - Vasculature - Innervation - TeachMeAnatomy. Published 2019. Accessed October 11, 2023. https://teachmeanatomy.info/head/organs/the-nose/nasal-cavity/

3.   Sobiesk JL, Munakomi S. Anatomy, head and neck, nasal cavity. Published online 2019.

4.   Born J, Lange T, Kern W, McGregor GP, Bickel U, Fehm HL. Sniffing neuropeptides: a transnasal approach to the human brain. *Nat Neurosci*. 2002;5(6):514-516. doi:10.1038/nn0602-849

5.   Xi J, Yuan JE, Zhang Y, Nevorski D, Wang Z, Zhou Y. Visualization and quantification of nasal and olfactory deposition in a sectional adult nasal airway cast. *Pharm Res*. 2016;33:1527-1541.

6.   Sacchetti C, Artusi M, Santi P, Colombo P. Caffeine microparticles for nasal administration obtained by spray drying. *Int J Pharm*. 2002;242(1-2):335-339.

7.   Russo P, Sacchetti C, Pasquali I, et al. Primary microparticles and agglomerates of morphine for nasal insufflation. *J Pharm Sci*. 2006;95(12):2553-2561.

8.   Torres LM, Trinidad J, Calderon E, Benitez D, Perelman M. Fentanyl pectin nasal spray for breakthrough cancer pain. *Int J Palliat Nurs*. 2015;21:114-116. doi:10.12968/ijpn.2015.21.3.114

9.   Targum SD, Daly E, Fedgchin M, Cooper K, Singh JB. Comparability of blinded remote and site-based assessments of response to adjunctive esketamine or placebo nasal spray in patients with treatment resistant depression. *J Psychiatr Res*. 2019;111:68-73.

10.   Cady R. A novel intranasal breath-powered delivery system for sumatriptan: a review of technology and clinical application of the investigational product AVP-825 in the treatment of migraine. *Expert Opin Drug Deliv*. 2015;12(9):1565-1577.

11.   Quintana D, Westlye L, Hope S, et al. Dose-Dependent Social-Cognitive Effects of Intranasal Oxytocin Delivered with Novel Breath Powered Device in Adults with Autism Spectrum Disorder: A Randomized Placebo-Controlled Double-Blind Crossover Trial. *Biol Psychiatry*. 2017;81(10):S167-S168.

12.   KA O. How nasal-spray vaccines could change the pandemic. *Nature*. 2022;609:240-242.

13.   Battistoni A, Lantier L, Tommaso A, et al. Nasal administration of recombinant Neospora caninum secreting IL-15/IL-15Rα inhibits metastatic melanoma development in lung. *J Immunother Cancer*. 2023;11. doi:10.1136/jitc-2023-006683

14.   Kundoor V, Dalby RN. Assessment of nasal spray deposition pattern in a silicone human nose model using a color-based method. *Pharm Res*. 2010;27:30-36.

15. Suman JD, Laube BL, Dalby R. Comparison of nasal deposition and clearance of aerosol generated by a nebulizer and an aqueous spray pump. *Pharm Res*. 1999;16(10):1648.

16. St. Martin MB, Hitzman CJ, Wiedmann TS, Rimell FL. Deposition of Aerosolized Particles in the Maxillary Sinuses before and after Endoscopic Sinus Surgery. *Am J Rhinol*. 2007;21(2):196-197. doi:10.2500/ajr.2007.21.2963

17. Merkus P, Ebbens FA, Muller B, Fokkens WJ. Influence of anatomy and head position on intranasal drug deposition. *European Archives of Oto-Rhino-Laryngology and Head & Neck*. 2006;263:827-832.

18. Jamil W, Alahwal A, Suman R, Naz F, Beech T. Do patients correctly use steroid nose spray? A patient-reported survey of the nasal spray technique and patient compliance. *Authorea Preprints*. Published online 2020.

19. Williams G, Suman JD. In Vitro Anatomical Models for Nasal Drug Delivery. *Pharmaceutics*. 2022;14(7). doi:10.3390/pharmaceutics14071353

20. Forbes B, Bommer R, Goole J, et al. A consensus research agenda for optimising nasal drug delivery. *Expert Opin Drug Deliv*. 2020;17(2):127-132.

21. Salade L, Wauthoz N, Goole J, Amighi K. How to characterize a nasal product. The state of the art of in vitro and ex vivo specific methods. *Int J Pharm*. 2019;561:47-65.

22. Djupesland PG, Messina JC, Mahmoud RA. Role of nasal casts for in vitro evaluation of nasal drug delivery and quantitative evaluation of various nasal casts. *Ther Deliv*. 2020;11(8):485-495.

23. Buttini F, Colombo P, Rossi A, Sonvico F, Colombo G. Particles and powders: tools of innovation for non-invasive drug administration. *Journal of controlled release*. 2012;161(2):693-702.

24. Lungare S, Bowen J, Badhan R. Development and evaluation of a novel intranasal spray for the delivery of amantadine. *J Pharm Sci*. 2016;105(3):1209-1220.

25. Nasal Cast - Alberta Idealised Nasal Inlet (AINI) | Copley Scientific. Accessed June 7, 2024. https://www.copleyscientific.com/inhaler-testing/realistic-throat-and-nasal-models/alberta-idealised-nasal-inlet-aini/

26. Penner MH. Basic principles of spectroscopy. *Food analysis*. Published online 2017:79-88.

27. Mygind N, Dahl R. Anatomy, physiology and function of the nasal cavities in health and disease. *Adv Drug Deliv Rev*. 1998;29(1):3-12. doi:https://doi.org/10.1016/S0169-409X(97)00058-6

28. Tai J, Han M, Lee D, Park IH, Lee SH, Kim TH. Different methods and formulations of drugs and vaccines for nasal administration. *Pharmaceutics*. 2022;14(5):1073.

29. Alagusundaram M, Chengaiah B, Gnanaprakash K, Ramkanth S, Chetty CM, Dhachinamoorthi D. Nasal drug delivery system-an overview. *Int J Res Pharm Sci*. 2010;1(4):454-465.

30. Salib RJ, Howarth PH. Safety and tolerability profiles of intranasal antihistamines and intranasal corticosteroids in the treatment of allergic rhinitis. *Drug Saf*. 2003;26:863-893.

31.   Formica ML, Real DA, Picchio ML, Catlin E, Donnelly RF, Paredes AJ. On a highway to the brain: A review on nose-to-brain drug delivery using nanoparticles. *Appl Mater Today*. 2022;29:101631. doi:https://doi.org/10.1016/j.apmt.2022.101631

32.   Maaz A, Blagbrough IS, De Bank PA. In vitro evaluation of nasal aerosol depositions: an insight for direct nose to brain drug delivery. *Pharmaceutics*. 2021;13(7):1079.

33.   Sachan N, Bahadur S, Sharma PK. Recent advances and novel approaches for nose to brain drug delivery for treatment of migraine. *Drug Deliv Lett*. 2019;9(3):182-198.

34.   Khatri DK, Preeti K, Tonape S, et al. Nanotechnological Advances for Nose to Brain Delivery of Therapeutics to Improve the Parkinson Therapy. *Curr Neuropharmacol*. 2023;21(3):493. doi:10.2174/1570159X20666220507022701

35.   Agrawal M, Saraf S, Saraf S, et al. Nose-to-brain drug delivery: An update on clinical challenges and progress towards approval of anti-Alzheimer drugs. *Journal of controlled release*. 2018;281:139-177.

36.   Teaima MH, El-Nadi MT, Hamed RR, El-Nabarawi MA, Abdelmonem R. Lyophilized nasal inserts of atomoxetine HCl solid lipid nanoparticles for brain targeting as a treatment of Attention-Deficit/Hyperactivity Disorder (ADHD): A pharmacokinetics study on rats. *Pharmaceuticals*. 2023;16(2):326.

37.   Alberto M, Paiva-Santos AC, Veiga F, Pires PC. Lipid and polymeric nanoparticles: successful strategies for nose-to-Brain drug delivery in the treatment of depression and anxiety disorders. *Pharmaceutics*. 2022;14(12):2742.

38.   Ullah I, Chung K, Bae S, et al. Nose-to-brain delivery of cancer-targeting paclitaxel-loaded nanoparticles potentiates antitumor effects in malignant glioblastoma. *Mol Pharm*. 2020;17(4):1193-1204.

39.   Shrewsbury SB. The Upper Nasal Space: Option for Systemic Drug Delivery, Mucosal Vaccines and "Nose-to-Brain." *Pharmaceutics*. 2023;15(6):1720. doi:10.3390/PHARMACEUTICS15061720/S1

40.   Zhang T, Dong B, Chen X, Qiu Z, Jiang R, Li W. Spray characteristics of pressure-swirl nozzles at different nozzle diameters. *Appl Therm Eng*. 2017;121:984-991. doi:https://doi.org/10.1016/j.applthermaleng.2017.04.089

41.   Rayleigh, Lord. On the dynamics of revolving fluids. *Proceedings of the Royal Society of London Series A, Containing Papers of a Mathematical and Physical Character*. 1917;93(648):148-154.

42.   Williams G, Suman JD. In vitro anatomical models for nasal drug delivery. *Pharmaceutics*. 2022;14(7):1353.

43.   Hughes R, Watterson J, Dickens C, Ward D, Banaszek A. Development of a nasal cast model to test medicinal nasal devices. *Proc Inst Mech Eng H*. 2008;222(7):1013-1022.

44.   Liu Y, Johnson MR, Matida EA, Kherani S, Marsan J. Creation of a standardized geometry of the human nasal cavity. *J Appl Physiol*. 2009;106(3):784-795.

45.   Xi J, Yuan JE, Zhang Y, Nevorski D, Wang Z, Zhou Y. Visualization and quantification of nasal and olfactory deposition in a sectional adult nasal airway cast. *Pharm Res*. 2016;33:1527-1541.

46.   3D Printing Guide: Types of 3D Printers, Materials, and Applications | Formlabs. Accessed June 6, 2024. https://formlabs.com/eu/3d-printers/

47.   Transparent Nasal Cavity Model LM-005 | Koken Co., Ltd. Accessed June 7, 2024. https://www.kokenmpc.co.jp/english/products/educational_medical_models/anatomical/lm-005.html

48.   Hagen M, Shanga G, Caron S, Debnath G. Nasal cast deposition for xylo-and oxymetazoline formulations using two different nasal pumps. Published online 2023.

49.   Deruyver L, Rigaut C, Lambert P, Haut B, Goole J. The importance of pre-formulation studies and of 3D-printed nasal casts in the success of a pharmaceutical product intended for nose-to-brain delivery. *Adv Drug Deliv Rev*. 2021;175:113826.

50.   Saijo R, Majima Y, Hyo N, Takano H. Particle Deposition of Therapeutic Aerosols in the Nose and Paranasal Sinuses after Transnasal Sinus Surgery: A Cast Model Study. *Am J Rhinol*. 2004;18(1):1-7. doi:10.1177/194589240401800101

51.   Djupesland PG, Skretting A, Winderen M, Holand T. Breath actuated device improves delivery to target sites beyond the nasal valve. *Laryngoscope*. 2006;116(3):466-472.

52.   Chen J, Finlay WH, Vehring R, Martin AR. Characterizing regional drug delivery within the nasal airways. *Expert Opin Drug Deliv*. Published online April 2, 2024. doi:10.1080/17425247.2024.2336494

53.   Chen JZ, Finlay WH, Martin A. In Vitro Regional Deposition of Nasal Sprays in an Idealized Nasal Inlet: Comparison with In Vivo Gamma Scintigraphy. *Pharm Res*. 2022;39(11):3021-3028. doi:10.1007/S11095-022-03388-7

54.   Calmet H, Oks D, Santiago A, et al. Validation and Sensitivity analysis for a nasal spray deposition computational model. *Int J Pharm*. 2022;626:122118.

55.   Barbarite E, Gadkaree SK, Melchionna S, Zwicker D, Lindsay RW. Computational Fluid Dynamics Modeling of Nasal Obstruction and Associations with Patient-Reported Outcomes. *Plast Reconstr Surg*. 2021;148(4):592E-600E. doi:10.1097/PRS.0000000000008328

56.   Davis SS, Hardy JG, Newman SP, Wilding IR. Gamma scintigraphy in the evaluation of pharmaceutical dosage forms. *Eur J Nucl Med*. 1992;19(11):971-986. doi:10.1007/BF00175865/METRICS

57.   Coura-Filho GB, Torres Silva de Oliveira M, Morais de Campos AL. Basic Principles of Scintigraphy and SPECT (Single-Photon Emission Computed Tomography). *Nuclear Medicine in Endocrine Disorders*. Published online 2022:9-14. doi:10.1007/978-3-031-13224-7_2

58.   Skretting A, Djupesland PG. A new method for scintigraphic quantification of deposition and clearance in anatomical regions of the human nose. *Nucl Med Commun*. 2009;30(8):629-638. doi:10.1097/MNM.0B013E32832C32B3

59.   Penner MH. Basic Principles of Spectroscopy. Published online 2017:79-88. doi:10.1007/978-3-319-45776-5_6

60.   Farias G, Shur J, Price R, Bielski E, Newman B. A Systematic Approach in the Development of the Morphologically-Directed Raman Spectroscopy Methodology for Characterizing Nasal Suspension Drug Products. *AAPS Journal*. 2021;23(4):1-12. doi:10.1208/S12248-021-00605-W/FIGURES/7

61.   Mitchell J, Bauer R, Lyapustina S, Tougas T, Glaab V. Non-impactor-based methods for sizing of aerosols emitted from orally inhaled and nasal drug products (OINDPs). *AAPS PharmSciTech*. 2011;12(3):965-988. doi:10.1208/S12249-011-9662-6/FIGURES/14

62.   Salade L, Wauthoz N, Goole J, Amighi K. How to characterize a nasal product. The state of the art of in vitro and ex vivo specific methods. *Int J Pharm*. 2019;561:47-65. doi:10.1016/J.IJPHARM.2019.02.026

63.   Tartrazine | C16H9N4Na3O9S2 | CID 164825 - PubChem. Accessed June 8, 2024. https://pubchem.ncbi.nlm.nih.gov/compound/Tartrazine#section=Experimental-Properties

64.   Sakai H, Watanabe Y, Sera T, Yokota H, Tanaka G. Visualization of particle deposition in human nasal cavities. *J Vis (Tokyo)*. 2015;18(2):349-357. doi:10.1007/S12650-014-0238-X/FIGURES/12

65.   Halderman AA, Stokken J, Sindwani R. The effect of middle turbinate resection on topical drug distribution into the paranasal sinuses. *Int Forum Allergy Rhinol*. 2016;6(10):1056-1061. doi:10.1002/ALR.21791

66.   Kundoor V, Dalby RN. Assessment of nasal spray deposition pattern in a silicone human nose model using a color-based method. *Pharm Res*. 2010;27(1):30-36. doi:10.1007/S11095-009-0002-4/FIGURES/7

67.   Yano A, Hamada K, Amagai K. Evaluation of Coating Film Formation Process Using the Fluorescence Method. *Coatings 2021, Vol 11, Page 1076*. 2021;11(9):1076. doi:10.3390/COATINGS11091076

68.   Kumar T, Verma K. A Theory Based on Conversion of RGB image to Gray image. *Int J Comput Appl*. 2010;7(2):7-10.

69.   Zhang MX, Verhoeven F, Ravensbergen P, et al. Improved Olfactory Deposition of Theophylline Using a Nanotech Soft Mist Nozzle Chip. *Pharmaceutics*. 2023;16(1):2.

70.   AAT Bioquest Inc. Spectrum [Calcein]. Published 2024. Accessed November 24, 2023. https://www.aatbio.com/fluorescence-excitation-emission-spectrum-graph-viewer/calcein

10. Addendum

A. Python code

In this segment the code is shown for the Intensity-Thickness calibration (A.1.) and Image analysis (A.2.). The actual scripts will be enclosed in Data_quantification_Mark_Scheeren zip file in the folder Python Code.

A.1. Intensity-thickness calibration algorithm

```python
import os
import cv2
import numpy as np
import pandas as pd
import matplotlib.pyplot as plt
from tkinter import Tk, filedialog


class Intensitycalibration:
    def __init__(self, image_path, row_start, row_end, column_start,
column_end):
        # Creates initial variables and image paths that will be used
throughout the script
        self.image_path = image_path
        self.original_image = cv2.imread(self.image_path)
        self.gray_image = self.original_image[:, :, 1]
        self.row_start = row_start
        self.row_end = row_end
        self.column_start = column_start
        self.column_end = column_end
        self.colors = ['#1f77b4', '#ff7f0e', '#2ca02c', '#d62728']
        self.containerlength = 77.3
        self.pixel_length = self.containerlength / (column_end -
column_start)
        self.angle_degrees = 1.778340378

    def create_output_folder(self):
        # Creates a folder to store the CSV files and images from the
analysis
        folder_name =
os.path.splitext(os.path.basename(self.image_path))[0]
        output_folder = os.path.join(os.getcwd(), folder_name)
        os.makedirs(output_folder, exist_ok=True)
        return output_folder

    def save_image(self, image, output_folder, image_name):
        # function to correctly store images
        image_path = os.path.join(output_folder, f'{image_name}.png')
        cv2.imwrite(image_path, image)
        print(f'Image saved: {image_path}')

    def get_intensity_per_row(self):
        # collects the intensity values for each row selected to analyse in
the image using the left and right
        # (column start and column end, respectively) values
        intensity_per_row = []
        for row_index in range(self.row_start, self.row_end + 1):
            row_intensities =
self.gray_image[row_index][self.column_start:self.column_end]
```

```python
                intensity_per_row.append(row_intensities)
        return intensity_per_row

    def depth_calculations(self):
        # this function calculates the depth steps for the container using
the left en right boundary set by manual detection

        opposite_lengths_per_row = []
        for row_index in range(self.row_start, self.row_end + 1):
            pixel_distance_x = np.arange(self.column_start,
self.column_end) - self.column_start
            opposite_lengths = []

            for pixel_distance in pixel_distance_x:
                # Calculate the length of the adjacent side in millimeters
                adjacent_length = pixel_distance * self.pixel_length

                # Convert the angle from degrees to radians
                angle_radians = np.radians(self.angle_degrees)

                # Calculate the length of the opposite side using the
tangent function
                opposite_length = adjacent_length * np.tan(angle_radians)

                opposite_lengths.append(opposite_length)

            opposite_lengths_per_row.append(opposite_lengths)

        return opposite_lengths_per_row

    def plot_intensity_per_row(self, output_folder, opposite_lengths,
intensity_per_row, plot_range=[15, -15]):
        #This function plots the intensity on y-axis and the thickness aka
the opposite side of the piramide on the x-axis
        #this only removes 15 pixels of the edges as it plots the raw data
        plt.figure(figsize=(10, 6))
        for row_index, intensities in enumerate(intensity_per_row):
            if plot_range:
                # Extract the plot range indices
                start_index, end_index = plot_range

plt.plot(opposite_lengths[row_index][start_index:end_index],
                         intensities[start_index:end_index],
                         label=f'Row {self.row_start + row_index}',
                         color=self.colors[row_index % len(self.colors)])
# Set color based on index
            else:
                plt.plot(opposite_lengths[row_index], intensities,
                         label=f'Row {self.row_start + row_index}',
                         color=self.colors[row_index % len(self.colors)])
# Set color based on index

        plt.xlabel('Opposite Side Length')
        plt.ylabel('Intensity')
        plt.title('Intensity vs. Opposite Side Length')
        plt.ylim(0, 255)
        plt.yticks(range(0, 256, 10))
        plt.savefig(os.path.join(output_folder,
'intensity_vs_opposite_lengths'), bbox_inches='tight')
        plt.close()
```

```python
    def plot_fitting_lines(self, output_folder, opposite_lengths,
intensity_per_row, plot_range=[50, -50]):
        # This function calculates the third order polynomial and creates a
plot to show the fitting lines
        coefficients_list = []
        plt.figure(figsize=(10, 6))
        for row_index, intensities in enumerate(intensity_per_row):
            # The for loop ensures that each line is analysed separately
            if plot_range:
                start_index, end_index = plot_range
                fit_opposite_lengths =
opposite_lengths[row_index][start_index:end_index]
                fit_intensities = intensities[start_index:end_index]
            else:
                fit_opposite_lengths = opposite_lengths[row_index]
                fit_intensities = intensities

            # Performs third-order polynomial regression
            fit = np.polyfit(fit_opposite_lengths, fit_intensities, 3)
            coefficients_list.append(fit)  # Stores coefficients for this
row
            fit_fn = np.poly1d(fit)

            # Plot the fitting line
            plt.plot(fit_opposite_lengths, fit_fn(fit_opposite_lengths),
                    label=f'Row {self.row_start + row_index}',
                    color=self.colors[row_index % len(self.colors)])  #
Set color based on index

        # Calculate the average coefficients for each degree term
        average_coefficients = np.mean(coefficients_list, axis=0)

        average_fit_fn = np.poly1d(average_coefficients)
        plt.plot(fit_opposite_lengths,
average_fit_fn(fit_opposite_lengths),
                label='Average Trendline', color='black', linestyle='--')

        plt.xlabel('Opposite Side Length')
        plt.ylabel('Intensity')
        plt.title('Fitting Lines for Each Row')
        plt.ylim(0, 255)
        plt.yticks(range(0, 256, 10))
        plt.savefig(os.path.join(output_folder, 'fitting_lines'),
bbox_inches='tight')
        plt.close()

        return coefficients_list, average_coefficients

    def plot_quadratic_fit(self, output_folder, opposite_lengths,
intensity_per_row, average_coefficients,
                        plot_range=[50, -50]):
        # This function determines the second order polynomial that
extrapolates the progression from the first value
        # of the third order polynomial and 0
        plt.figure(figsize=(20, 12))
        for row_index, intensities in enumerate(intensity_per_row):
            if plot_range:
                start_index, end_index = plot_range
                fit_opposite_lengths =
opposite_lengths[row_index][start_index:end_index]
                fit_intensities = intensities[start_index:end_index]
```

```python
        else:
            fit_opposite_lengths = opposite_lengths[row_index]
            fit_intensities = intensities

            # Plot original data
            plt.plot(fit_opposite_lengths, fit_intensities,
                     label=f'Row {self.row_start + row_index}',
                     color=self.colors[row_index % len(self.colors)])

    # Generate the average polynomial fit function
    average_fit_fn = np.poly1d(average_coefficients)

    # Plot the average polynomial fit
    plt.plot(fit_opposite_lengths,
average_fit_fn(fit_opposite_lengths),
             label='Average Polynomial Fit', color='blue', linestyle='-
')

    # Calculate the first value of the average polynomial fit
    first_value_x = fit_opposite_lengths[0]
    first_value_y = average_fit_fn(first_value_x)


    # Generate quadratic fit points from (0, 0) to (first_value_x,
first_value_y)
    quadratic_fit_x = [0, first_value_x / 2, first_value_x]
    quadratic_fit_y = [0, first_value_y / 2, first_value_y]

    # Calculate the quadratic fit coefficients
    quadratic_fit_coefficients = np.polyfit(quadratic_fit_x,
quadratic_fit_y, 2)

    # Generate the quadratic fit function
    quadratic_fit_fn = np.poly1d(quadratic_fit_coefficients)

    # Plot the quadratic fit line
    fit_x = np.linspace(0, first_value_x, 100)
    plt.plot(fit_x, quadratic_fit_fn(fit_x), label='Quadratic Fit',
color='black', linestyle='--')

    plt.xlabel('Thickness of fluorescent solution (mm)', fontsize=32)
    plt.ylabel('Intensity', fontsize=32)
    plt.title('Different thickness of container', fontsize=34,
fontweight='bold', pad=32)
    plt.ylim(0, 255)
    plt.yticks(range(0, 256, 10), fontsize=18)
    plt.xticks(fontsize=18)

    plt.savefig(os.path.join(output_folder,
'quadratic_and_average_polynomial_fit'), bbox_inches='tight')
    plt.close()

    return quadratic_fit_coefficients, quadratic_fit_y, first_value_x,
first_value_y

def run_analysis(self, image_filename):
    # This function ensures that when running the code each function is
called correctly and stores the
    # polynomials to the correct CSV file.
    output_folder = self.create_output_folder()
    intensity_per_row = self.get_intensity_per_row()
```

```python
        opposite_lengths = self.depth_calculations()
        self.plot_intensity_per_row(output_folder, opposite_lengths,
intensity_per_row)
        coefficients_list, average_coefficients =
self.plot_fitting_lines(output_folder, opposite_lengths,

intensity_per_row)

        # Plot quadratic fit and get the coefficients
        quadratic_fit_coefficients, quadratic_fit_y, first_value_x,
first_value_y = self.plot_quadratic_fit(output_folder, opposite_lengths,

intensity_per_row,

average_coefficients)

        # Get the original file name without extension
        original_filename = os.path.splitext(image_filename)[0]

        # Save intensity_per_row to a CSV file
        intensity_csv_filename =
f"{original_filename}_intensity_per_row.csv"
        intensity_df = pd.DataFrame(intensity_per_row)
        intensity_df.to_csv(os.path.join(output_folder,
intensity_csv_filename), index=False)

        # Save opposite_lengths to a CSV file
        opposite_lengths_csv_filename =
f"{original_filename}_opposite_lengths.csv"
        opposite_lengths_df = pd.DataFrame(opposite_lengths)
        opposite_lengths_df.to_csv(os.path.join(output_folder,
opposite_lengths_csv_filename), index=False)

        # Save coefficients_list to a CSV file
        coefficients_csv_filename =
f"{original_filename}_coefficients_list.csv"
        coefficients_df = pd.DataFrame(coefficients_list)
        coefficients_df.to_csv(os.path.join(output_folder,
coefficients_csv_filename), index=False)

        # Save average_coefficients to a CSV file
        average_coefficients_csv_filename =
f"{original_filename}_average_coefficients_polynominal.csv"
        average_coefficients_df = pd.DataFrame({'Average_coefficients':
average_coefficients})
        average_coefficients_df.to_csv(os.path.join(output_folder,
average_coefficients_csv_filename), index=False)

        # Save quadratic_fit_coefficients to a CSV file
        quadratic_fit_coefficients_csv_filename =
f"{original_filename}_quadratic_fit_coefficients.csv"
        quadratic_fit_coefficients_df =
pd.DataFrame({'Quadratic_fit_coefficients': quadratic_fit_coefficients})
        quadratic_fit_coefficients_df.to_csv(os.path.join(output_folder,
quadratic_fit_coefficients_csv_filename),
                                             index=False)

        print("Data saved to CSV files:", intensity_csv_filename,
opposite_lengths_csv_filename,
              coefficients_csv_filename, average_coefficients_csv_filename,
quadratic_fit_coefficients_csv_filename)
```

```python
        print('first intensity value', first_value_y)
        print('first depth value', first_value_x)


# Get image path from the user.
root = Tk()
root.withdraw()
file_paths = filedialog.askopenfilenames(title="Select Images",
filetypes=[("Image Files", "*.jpg;*.png;*.jpeg")])
root.destroy()

if not file_paths:
    print("No files selected. Exiting.")
else:
    for image_path in file_paths:
        # Input row and column ranges
        row_start = int(input("Enter the starting row index: "))
        row_end = int(input("Enter the ending row index: "))
        column_start = int(input("Enter the starting column index: "))
        column_end = int(input("Enter the ending column index: "))
        image_filename = os.path.basename(image_path)
        image_analysis = Intensitycalibration(image_path, row_start,
row_end, column_start, column_end)
        image_analysis.run_analysis(image_filename)
```

A.2. Image analysis algorithm

```python
import os
import cv2
import numpy as np
import matplotlib.pyplot as plt
import pandas as pd
from tkinter import Tk, filedialog


class ImageAnalysis:
    def __init__(self, image_path):
        # initialisation of the algorithm and establishes pathfile linking.
        self.image_path = image_path
        self.original_image = cv2.imread(self.image_path)
        if self.original_image is None:
            raise ValueError(f"Image at path {image_path} could not be
loaded.")
        self.gray_image = self.original_image[:, :, 1]  # the grey image is
created using the green spectrum

    def create_output_folder(self):
        # Creates a folder to store the results
        folder_name =
os.path.splitext(os.path.basename(self.image_path))[0]
        output_folder = os.path.join(os.getcwd(), folder_name)
        os.makedirs(output_folder, exist_ok=True)
        return output_folder

    def save_image(self, image, output_folder, image_name):
        # A function that helps store images correctly
        image_path = os.path.join(output_folder, f'{image_name}.png')
        cv2.imwrite(image_path, image)
        print(f'Image saved: {image_path}')

    @staticmethod
    def load_polynomial_coefficients():
        # This function prompts the user to load the third polynomial data
        print('Loading polynomial coefficients...')
        root = Tk()
        root.withdraw()
        csv_paths = filedialog.askopenfilenames(title="Select Polynomial
Coefficients CSV files",
                                                filetypes=[("CSV Files",
"*.csv")])
        root.destroy()

        if not csv_paths:
            print("No polynomial coefficients CSV files selected.")
            return None

        polynomial_coefficients_data = []

        for csv_path in csv_paths:
            folder_name = os.path.basename(os.path.splitext(csv_path)[0])
            try:
                avg_coefficients_df = pd.read_csv(csv_path, header=None)
                if len(avg_coefficients_df) >= 4:
                    a3, a2, a1, a0 = avg_coefficients_df.iloc[1, 0],
avg_coefficients_df.iloc[2, 0], \
                        avg_coefficients_df.iloc[3, 0],
```

```python
avg_coefficients_df.iloc[4, 0]
                    polynomial_coefficients_data.append((a3, a2, a1, a0,
folder_name))
                else:
                    print(f"CSV file {csv_path} does not contain the
required number of coefficients.")
            except Exception as e:
                print(f"Error loading polynomial coefficients from
{csv_path}: {e}")

        return polynomial_coefficients_data

    @staticmethod
    def load_second_order_coefficients():
        # This function prompts the user to load the second order
polynomial data
        print('Loading second order coefficients...')
        root = Tk()
        root.withdraw()
        csv_paths = filedialog.askopenfilenames(title="Select Second Order
Coefficients CSV files",
                                                filetypes=[("CSV Files",
"*.csv")])
        root.destroy()

        if not csv_paths:
            print("No second-order coefficients CSV files selected.")
            return None

        second_order_coefficients_data = []

        for csv_path in csv_paths:
            folder_name = os.path.basename(os.path.splitext(csv_path)[0])
            try:
                avg_coefficients_df = pd.read_csv(csv_path, header=None)
                if len(avg_coefficients_df) >= 3:
                    a2, a1, a0 = avg_coefficients_df.iloc[1, 0],
avg_coefficients_df.iloc[2, 0], \
                        avg_coefficients_df.iloc[3, 0]
                    second_order_coefficients_data.append((a2, a1, a0,
folder_name))
                else:
                    print(f"CSV file {csv_path} does not contain the
required number of coefficients.")
            except Exception as e:
                print(f"Error loading second-order coefficients from
{csv_path}: {e}")

        return second_order_coefficients_data

    def calculate_depth_map(self, image, polynomial_coefficients_data,
second_order_coefficients_data):
        # This function calculates the different depth maps for each
algorithm separately and combined resulting in
        # thickness of the fluorescent dye
        print('Calculating depth map')
        depth_map = np.zeros_like(image, dtype=np.float32)  # stores all
data
        depth_map1 = np.zeros_like(image, dtype=np.float32)  # stores only
the second order polynomial data
        depth_map2 = np.zeros_like(image, dtype=np.float32)  # stores only
```

```
the third order polynomial data

        for i in range(image.shape[0]):
            for j in range(image.shape[1]):
                intensity = float(image[i, j])

                if intensity < 5:
                    # below 5 is deemed background noise and will set all
information to 0
                    depth_map[i, j] = 0
                    depth_map1[i, j] = 0
                    depth_map2[i, j] = 0
                elif 5 <= intensity <= 52 and
len(second_order_coefficients_data) > 0:
                    # The second order polynomial is from 0, which is
established to be below 5 to the first value of
                    # the calibration with the third order polynomial. As
this study used 725 as calibration that
                    # resulted in 53 being the first intensity value of the
third polynomial.
                    # With different calibration data these limits will
need to be adjusted.
                    a2, a1, a0, _ = second_order_coefficients_data[0]
                    a2 = float(a2)
                    a1 = float(a1)
                    a0 = float(a0)

                    coeffs = [a2, a1, (a0 - intensity)]
                    roots = np.roots(coeffs)
                    real_roots = roots[np.isreal(roots)]
                    real_roots = real_roots.real
                    valid_roots = real_roots[real_roots > 0]

                    if valid_roots.size > 0:
                        depth_map[i, j] = np.min(valid_roots)
                        depth_map1[i, j] = np.min(valid_roots)
                        depth_map2[i, j] = 0
                    else:
                        print('No valid roots for second-order polynomial')
                        exit(9)
                elif intensity > 52 and len(polynomial_coefficients_data) >
0:
                    # All data above this limit from which the third
polynomial is used to quantify thickness of the
                    # fluorescent dye
                    a, b, c, d, _ = polynomial_coefficients_data[0]
                    a = float(a)
                    b = float(b)
                    c = float(c)
                    d = float(d)
                    coeffs = [a, b, c, (d - intensity)]
                    roots = np.roots(coeffs)
                    real_roots = roots[np.isreal(roots)]
                    real_roots = real_roots.real
                    valid_roots = real_roots[real_roots > 0]

                    if valid_roots.size > 0:
                        depth_map[i, j] = np.min(valid_roots)
                        depth_map1[i, j] = 0
                        depth_map2[i, j] = np.min(valid_roots)
                    else:
```

```python
                        print('No valid roots for cubic polynomial')
                        exit(9)

        return depth_map, depth_map1, depth_map2

    def threshold_analysis(self, thresholds):
        # This function performs small analysis to divide the data surface
coverage for the two intensity ranges
        binary_images = [cv2.inRange(self.gray_image, low, high) for low,
high in thresholds]
        intensity_thresholds = [cv2.bitwise_and(self.gray_image,
self.gray_image, mask=binary_image) for binary_image in
                                binary_images]
        histograms = [cv2.calcHist([binary_image], [0], None, [256], [0,
256]) for binary_image in binary_images]
        pixel_area = [(np.sum(binary_image == 255)) * 0.001187295 for
binary_image in binary_images]
        percentages = [(np.sum(binary_image == 255) / (binary_image.size))
* 100 for binary_image in binary_images]
        total_percentage = sum(percentages)
        return binary_images, intensity_thresholds, histograms,
percentages, total_percentage, pixel_area

    def visualize_threshold_windows(self, binary_images, thresholds,
output_folder):
        # Creates the separate threshold images
        fig, axes = plt.subplots(2, 1, figsize=(12, 8))
        for i, (binary_image, ax) in enumerate(zip(binary_images,
axes.flatten()), 1):
            low_limit, high_limit = thresholds[i - 1]
            ax.imshow(binary_image, cmap='gray')
            ax.set_title(f'Threshold Window {i}\nLow: {low_limit}, High:
{high_limit}')
            ax.axis("off")

        combined_filename = os.path.join(output_folder,
'threshold_windows_combined.png')
        plt.savefig(combined_filename, bbox_inches='tight')
        plt.close()

    def save_threshold_images(self, binary_images, thresholds,
output_folder):
        # Stores the images for each threshold
        for i, binary_image in enumerate(binary_images, 1):
            low_limit, high_limit = thresholds[i - 1]
            threshold_filename =
f'Threshold_Window_{i}_Low_{low_limit}_High_{high_limit}'
            self.save_image(binary_image, output_folder,
threshold_filename)

    def visualize_depth_map(self, depth_map, output_folder,
original_image_path):
        # Creates the Depth map image for all data
        print("creating depth map")

        # Load the original image
        original_image = cv2.imread(original_image_path)
        if original_image is None:
            raise ValueError(f"Image at path {original_image_path} could
not be loaded.")
```

```python
        # Extract the blue channel
        blue_channel = original_image[:, :, 0]

        # Prepare the depth map
        depth_map_with_nan = np.copy(depth_map)
        depth_map_with_nan[depth_map_with_nan == 0] = np.nan

        # Create the colormap for the depth map
        cmap = plt.cm.viridis
        cmap.set_bad(color='black')

        # Create a figure and axis
        fig, ax = plt.subplots(figsize=(24, 18))

        # Display the blue channel image in the background
        ax.imshow(blue_channel)  # Use alpha to blend

        # Overlay the depth map
        depth_map_img = ax.imshow(depth_map_with_nan, cmap=cmap, alpha=0.8)
# Use alpha to blend

        # Add colorbar and title
        colorbar = fig.colorbar(depth_map_img, ax=ax, label='Thickness
(mm)',
                                ticks=np.linspace(0, np.nanmax(depth_map),
10))

        # Set font size for colorbar ticks
        colorbar.ax.tick_params(labelsize=24)

        # Set font size for colorbar label
        colorbar.set_label('Thickness (mm)', fontsize=32, labelpad=20)

        ax.set_title('Full Depth Map', fontsize=34, fontweight='bold',
pad=32)
        plt.xticks([])
        plt.yticks([])

        colorbar.ax.set_aspect('auto')

        # Save the figure
        plt.savefig(os.path.join(output_folder,
'depth_map_with_background.png'), bbox_inches='tight')
        plt.close()

    def visualize_depth_map1(self, depth_map1, output_folder,
original_image_path):
        # Creates the depth map for the lower intensities
        print("creating depth map1")

        # Load the original image
        original_image = cv2.imread(original_image_path)
        if original_image is None:
            raise ValueError(f"Image at path {original_image_path} could
not be loaded.")

        # Extract the blue channel
        blue_channel = original_image[:, :, 0]

        # Prepare the depth map
        depth_map_with_nan = np.copy(depth_map1)
```

```python
        depth_map_with_nan[depth_map_with_nan == 0] = np.nan

        # Create the colormap for the depth map
        cmap = plt.cm.viridis
        cmap.set_bad(color='black')

        # Create a figure and axis
        fig, ax = plt.subplots(figsize=(24, 18))

        # Display the blue channel image in the background
        ax.imshow(blue_channel)  # Use alpha to blend

        # Overlay the depth map
        depth_map_img = ax.imshow(depth_map_with_nan, cmap=cmap, alpha=0.8)
# Use alpha to blend

        # Add colorbar and title
        colorbar = fig.colorbar(depth_map_img, ax=ax, label='Thickness
(mm)',
                                ticks=np.linspace(0, np.nanmax(depth_map1),
10))

        # Set font size for colorbar ticks
        colorbar.ax.tick_params(labelsize=24)

        # Set font size for colorbar label
        colorbar.set_label('Thickness (mm)', fontsize=32, labelpad=20)

        ax.set_title('Depth Map < 0.05 mm', fontsize=34, fontweight='bold',
pad=32)
        plt.xticks([])
        plt.yticks([])

        colorbar.ax.set_aspect('auto')

        # Save the figure
        plt.savefig(os.path.join(output_folder,
'depth_map1_with_background.png'), bbox_inches='tight')
        plt.close()

    def visualize_depth_map2(self, depth_map2, output_folder,
original_image_path):
        # Creates the depth map for higher intensities
        print("creating depth map2")

        # Load the original image
        original_image = cv2.imread(original_image_path)
        if original_image is None:
            raise ValueError(f"Image at path {original_image_path} could
not be loaded.")

        # Extract the blue channel
        blue_channel = original_image[:, :, 0]

        # Prepare the depth map
        depth_map_with_nan = np.copy(depth_map2)
        depth_map_with_nan[depth_map_with_nan == 0] = np.nan

        # Create the colormap for the depth map
        cmap = plt.cm.viridis
        cmap.set_bad(color='black')
```

```python
        # Create a figure and axis
        fig, ax = plt.subplots(figsize=(24, 18))

        # Display the blue channel image in the background
        ax.imshow(blue_channel)  # Use alpha to blend

        # Overlay the depth map
        depth_map_img = ax.imshow(depth_map_with_nan, cmap=cmap, alpha=0.8)
# Use alpha to blend

        # Add colorbar and title
        colorbar = fig.colorbar(depth_map_img, ax=ax, label='Thickness
(mm)',
                                ticks=np.linspace(0, np.nanmax(depth_map2),
11))

        # Set font size for colorbar ticks
        colorbar.ax.tick_params(labelsize=24)

        # Set font size for colorbar label
        colorbar.set_label('Thickness (mm)', fontsize=32, labelpad=20)

        ax.set_title('Depth Map > 0.05 mm', fontsize=34, fontweight='bold',
pad=32)
        plt.xticks([])
        plt.yticks([])

        colorbar.ax.set_aspect('auto')

        # Save the figure
        plt.savefig(os.path.join(output_folder,
'depth_map2_with_background.png'), bbox_inches='tight')
        plt.close()

    def calculate_total_volume(self, depth_map, depth_map1, depth_map2):
        print("Calculating Total Volume")
        total_volume = np.sum(depth_map * 0.001187295)
        total_volume1 = np.sum(depth_map1 * 0.001187295)
        total_volume2 = np.sum(depth_map2 * 0.001187295)
        input_volume = input("Please enter the actual volume: ")
        Recoverpercentage = ((total_volume - float(input_volume)) /
float(input_volume)) * 100
        return total_volume, total_volume1, total_volume2,
Recoverpercentage

    def run_analysis(self):
        # This function is the main script that runs all separate functions
and their respective inputs. This manages
        # the flow of information needed for each step
        try:
            thresholds = [(5, 52), (53, 256)]
            output_folder = self.create_output_folder()
            print("Folder created:", output_folder)

            polynomial_coefficients_data =
self.load_polynomial_coefficients()
            if not polynomial_coefficients_data:
                print("Error loading polynomial coefficients. Exiting.")
                return
            print(polynomial_coefficients_data)
```

```python
            second_order_coefficients_data =
self.load_second_order_coefficients()
            if not second_order_coefficients_data:
                print("Error loading second-order coefficients. Exiting.")
                return
            print(second_order_coefficients_data)

            binary_images, intensity_thresholds, histograms, percentages,
total_percentage, pixel_area = self.threshold_analysis(
                thresholds)
            print("Threshold analysis performed")

            self.visualize_threshold_windows(binary_images, thresholds,
output_folder)
            self.save_threshold_images(binary_images, thresholds,
output_folder)
            depth_map, depth_map1, depth_map2 =
self.calculate_depth_map(self.gray_image, polynomial_coefficients_data,

second_order_coefficients_data)
            self.visualize_depth_map(depth_map, output_folder,
self.image_path)
            self.visualize_depth_map1(depth_map1, output_folder,
self.image_path)
            self.visualize_depth_map2(depth_map2, output_folder,
self.image_path)
            total_volume, total_volume1, total_volume2, Recoverypercentage
= self.calculate_total_volume(depth_map,

depth_map1,

depth_map2)
            print("Area covered per threshold:", pixel_area, "mm^2")
            print("Percentage per threshold:", percentages, "%")
            print("Total percentage coated:", total_percentage, "%")
            print("Total Volume:", total_volume, "mm^3")
            print("Total Volume1:", total_volume1, "mm^3")
            print("Total Volume2:", total_volume2, "mm^3")
            print("Recovery Percentage:", Recoverypercentage, "%")
        except Exception as e:
            print(f"An error occurred during analysis: {e}")


root = Tk()
root.withdraw()
file_paths = filedialog.askopenfilenames(title="Select Images",
filetypes=[("Image Files", "*.jpg;*.png;*.jpeg")])
root.destroy()

if not file_paths:
    print("No files selected. Exiting.")
else:
    for image_path in file_paths:
        try:
            image_analysis = ImageAnalysis(image_path)
            image_analysis.run_analysis()
        except ValueError as e:
            print(e)
```

B. Images acquired from volume qualification experiments

Displayed here are supportive images for section 4.3. All collected images are enclosed in the zip file named Data_quantification_Mark_Scheeren.

B.1 Flat surface analysis

Additional analysis of the flat surface showing experiment 3 as support to experiment 4. All experiments images are found in the folder Flat surface analysis.

B.1.1 Experiment 3 (DSC_0743)

B.1.1.1 Raw image

Figure 32: Raw image of DSC_0743, flat surface coated with 0.2mg/ml calcein

B.1.1.2 Depth Maps low and high-intensity
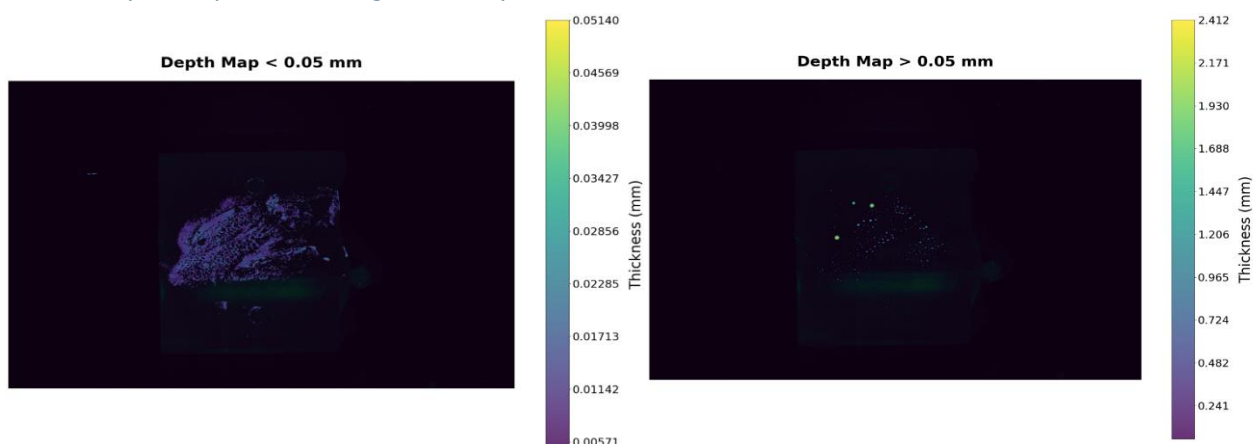
Figure 33: The depth maps for thickness < 0.05 mm (left) and thicker deposition (right) from experiment 3

B.1.1.3 Full depth map
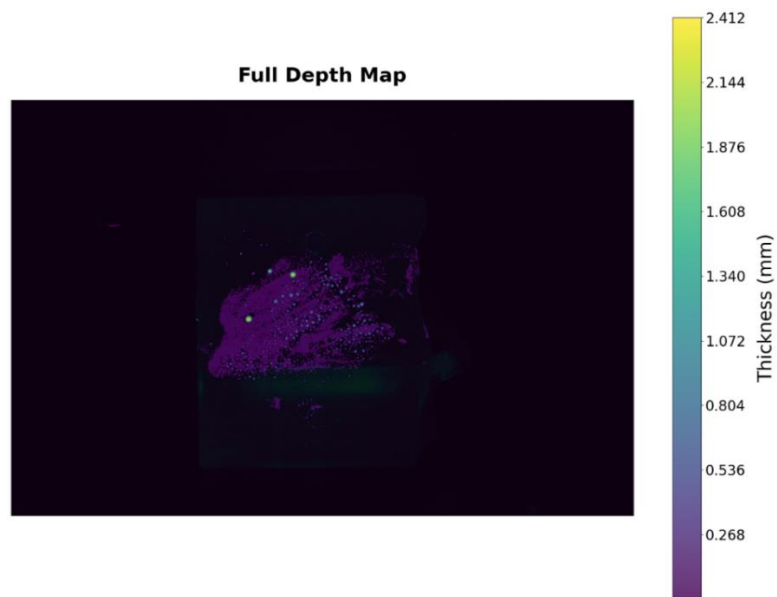
Figure 34: Full depth map of experiment 3

B.2 Koken Model analysis

This section contains the low and high-intensity dept maps of experiment 15. All experiment images obtained from this analysis can be found in the folder Koken Model Analysis of the enclosed zip file.

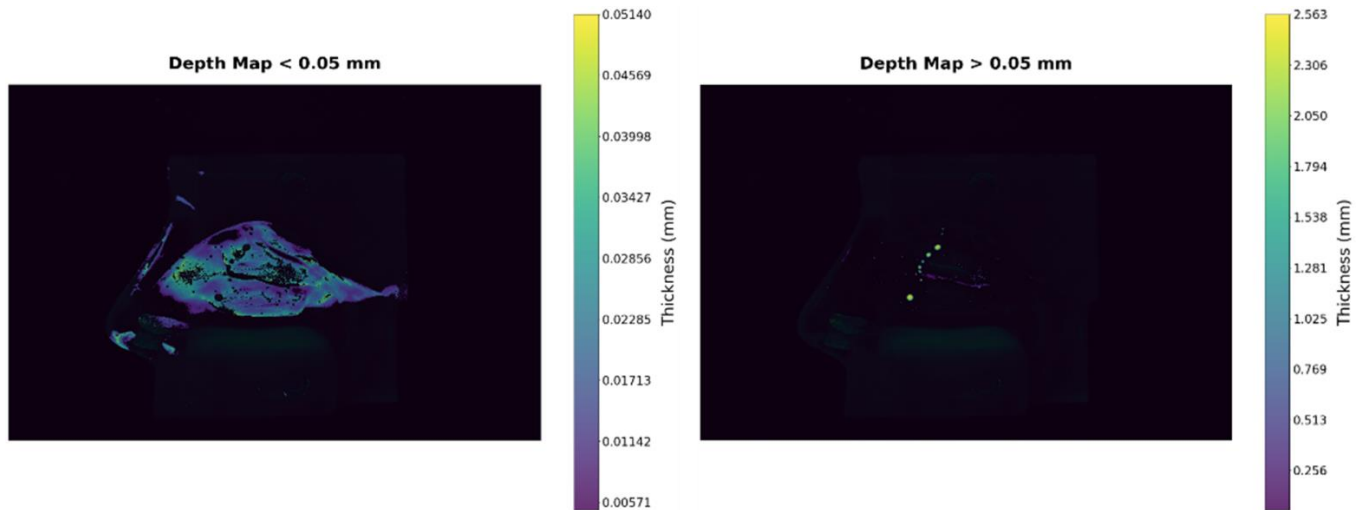## B.2.1 Depth maps Low and High-intensity experiment 15

Figure 35: The depth maps for thickness < 0.05 mm (left) and thicker deposition (right) from experiment 15

B.3 3D Mask analysis

Here are the raw image and low and high-intensity depth maps from experiment 15 cropped. All experiments analysed in this manner can be found in the folder 3D mask.
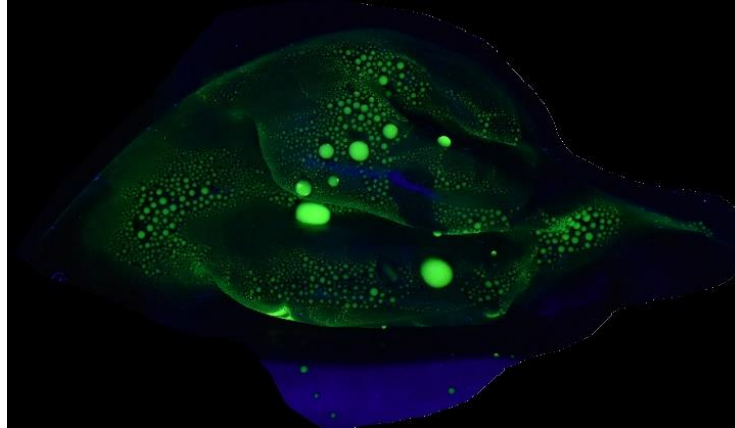
B.3.1 Raw image cropped experiment 15 cropped

Figure 36: Raw image of cropped DSC_0755, flat surface coated with 0.2mg/ml calcein

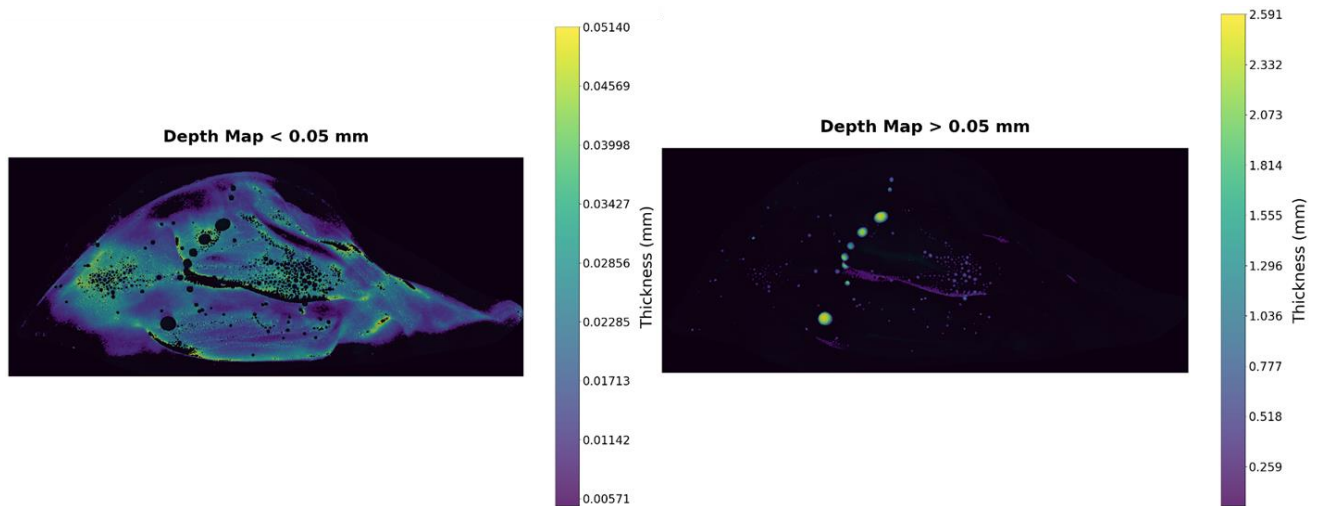### B.3.2 Depth maps Low and High-intensity experiment 15 cropped

Figure 37: The depth maps for thickness < 0.05 mm (left) and thicker deposition (right) from experiment 15 cropped

C. Quantification of aerosol deposition

In this section, supportive images from the aerosol deposition are displayed. All images can be found in the Folder Aerosol deposition of the zip file Data_quantification_Mark_Scheeren, where the swirl nozzle experiments are found in the subfolder swirl nozzle and soft mist atomizer in the subfolder Soft Mist.

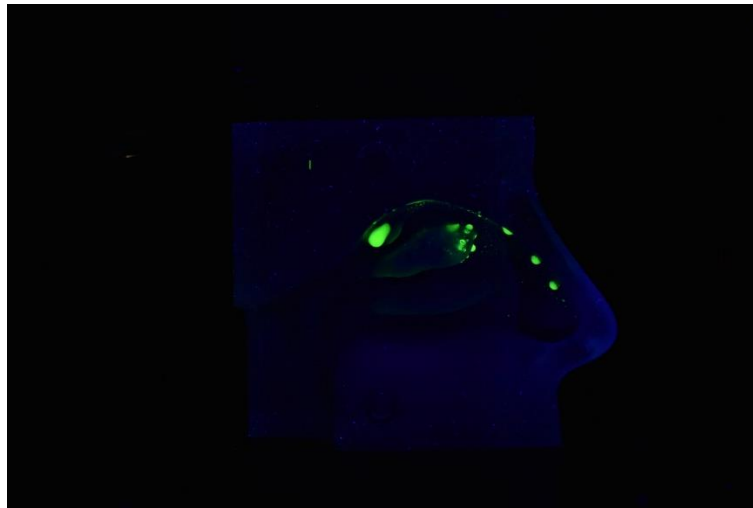## C. 1. Swirl nozzle 15 L/min airflow

C. 1.1 Raw image

Figure 38: The raw image of the third aerosol deposition created by a traditional swirl nozzle with 15 L/min airflow.
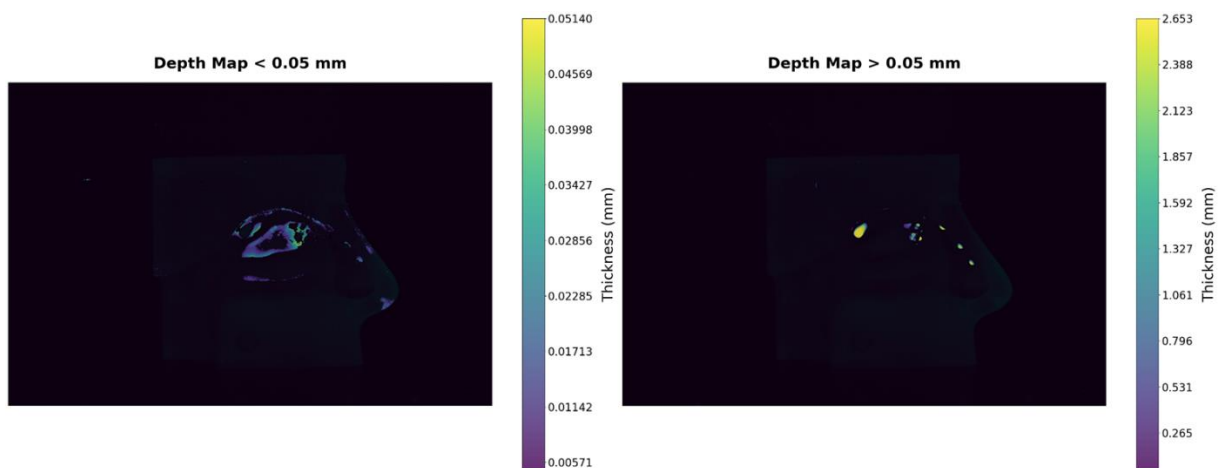
C. 1.2 Depth Maps low and high-intensity

Figure 39: The depth maps for thickness < 0.05 mm (left) and thicker deposition (right) from the third deposition created with the Swirl nozzle nasal spray with 15 L/min.

C. 2. Soft Mist Spray nozzle 15L/min airflow

C. 2.1 Raw image

Figure 40: The raw image of the third aerosol deposition created by a soft mist nozzle with 15 L/min airflow.

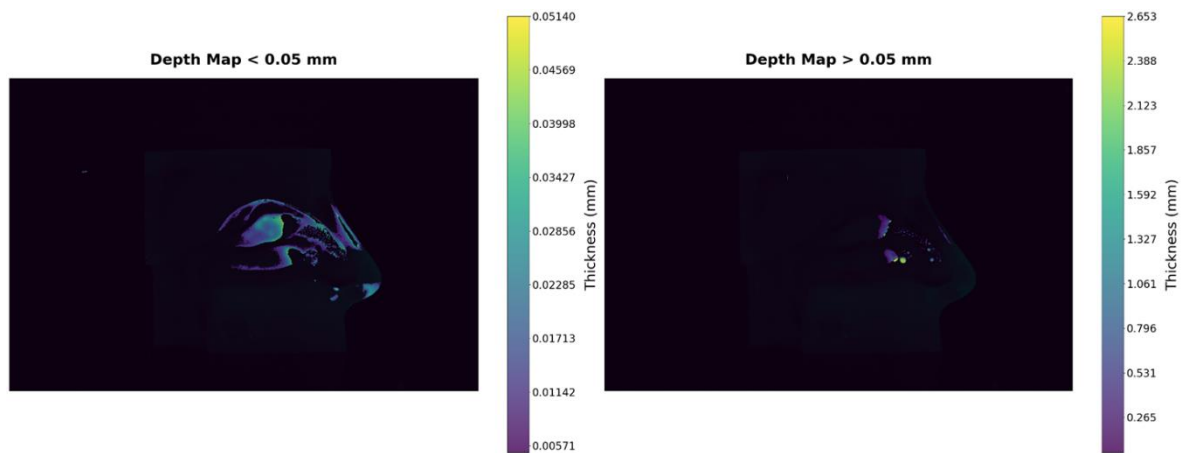### C. 2.2 Depth Maps low and high-intensity

Figure 41: The depth maps for thickness < 0.05 mm (left) and thicker deposition (right) from the third deposition created with the Soft Mist atomizer with 15 L/min.